Supporting Information

High-Performance Aprotic Li–CO_2 Battery Enabled by the Ru Heterophase Catalyst

Liang Sun[a], Qinfen Gu[b], Jodie A. Yuwono[a], Jingwen Zhou[c], Bernt Johannessen[b, d], Lingfei Zhao[d], Chaofeng Zhang[e], Guanjie Li[a], Zaiping Guo[a, *], Shilin Zhang[a, *]

a. School of Chemical Engineering, The University of Adelaide, Adelaide, 5000, Australia
b. Australian Synchrotron, ANSTO, Clayton, 3168, Australia
c. Department of Chemistry, City University of Hong Kong, Kowloon, Hong Kong SAR, 999077, China
d. Institute for Superconducting & Electronic Materials, University of Wollongong, Wollongong, NSW 2500, Australia
e. Institutes of Physical Science and Information Technology, Anhui University, Hefei, 230601 China

Corresponding author: shilin.zhang01@adelaide.edu.au (S.Z); zaiping.guo@adelaide.edu.au (Z.G)

Figure S1

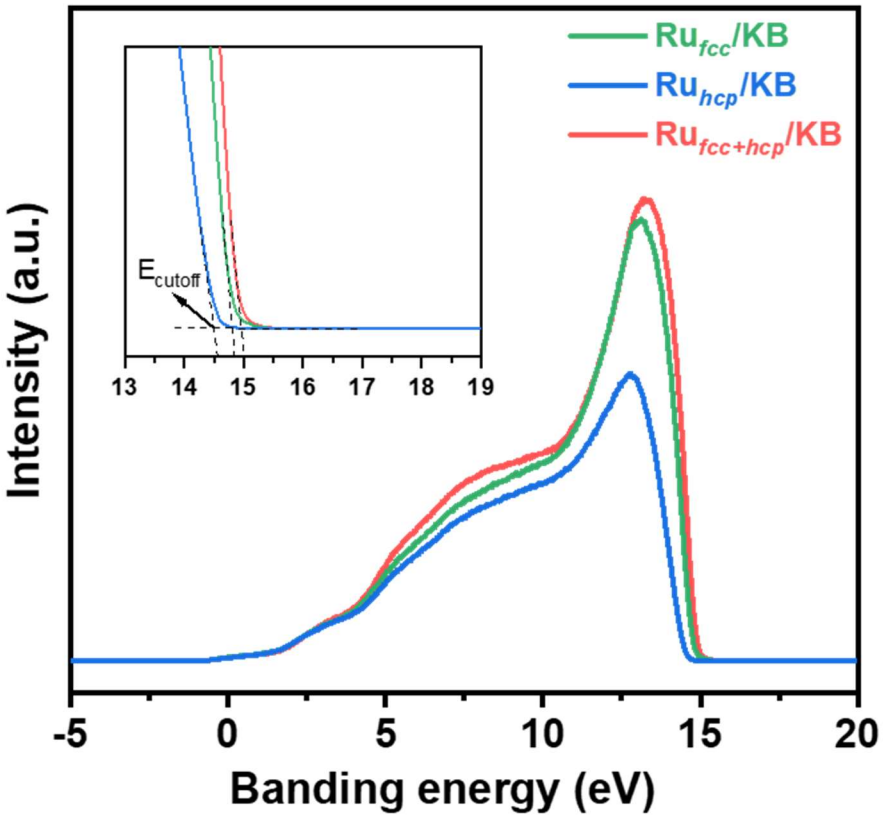

Figure S1. The local magnification of UPS of Ru_{fcc}/KB (5.54 eV) Ru_{hcp}/KB (5.84 eV) and $Ru_{fcc+hcp}$/KB (5.36 eV).

Ultraviolet photo-electron spectroscopy (UPS) were recorded after Ar^+ sputtering at 2 kV for 45 s to minimize surface contamination. A He discharge lamp (He I, $h\nu$ = 21.22 eV) was used for UPS measurements, with a sample bias of -10 eV. The Au $4f_{7/2}$ core-level signal at a binding energy of 83.8 eV served as the reference for electron energy calibration. The work function was determined using the equation $\phi = h\nu - (E_{cutoff} - E_{Fermi\ level})$, where $h\nu$ corresponds to the UV photon energy (21.22 eV), E_{cutoff} indicates the final state energy, and $E_{Fermi\ level}$ represents the initial state energy.[1] A lower work function reduces the energetic barrier for catalysts to transfer surface electrons to adsorbed CO_2, facilitating intermediate formation—the rate-determining step in CRR. This work function modulation strategy offers valuable insight into designing efficient electrocatalysts for enhanced CRR performance.[2]

Figure S2

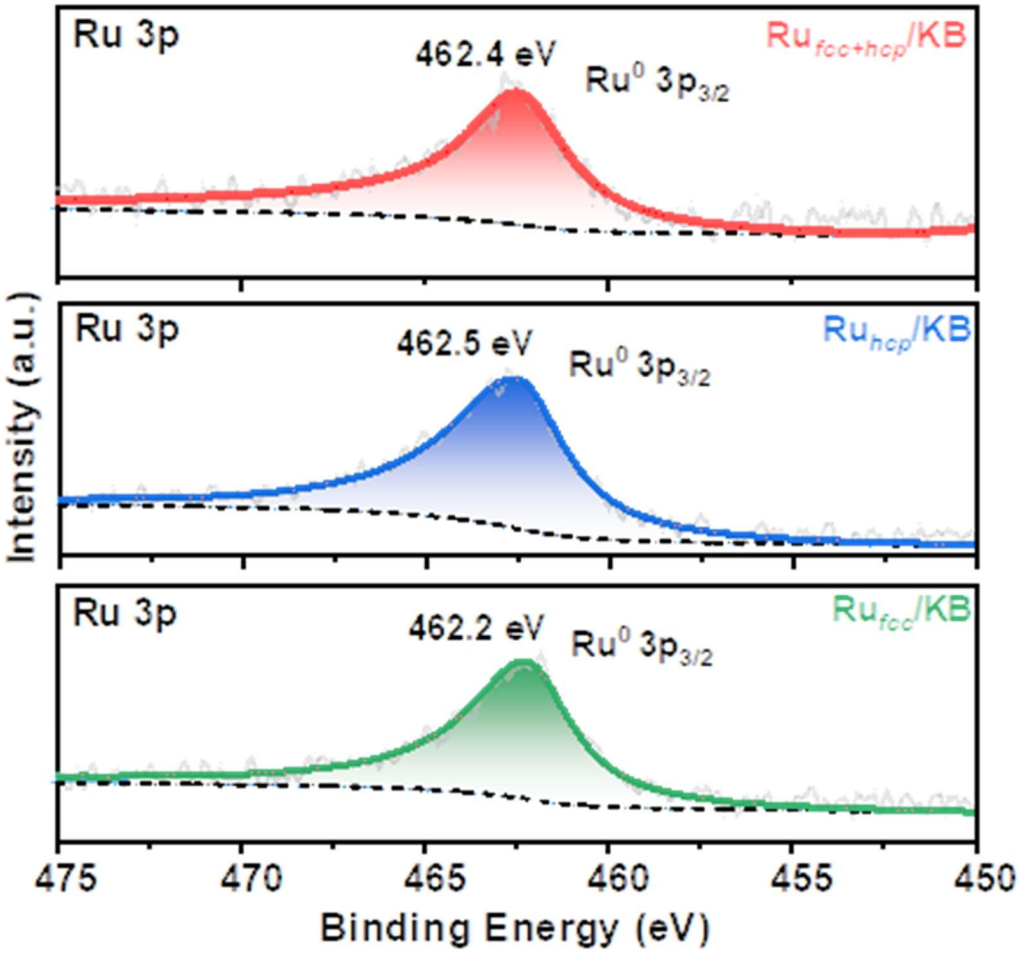

Figure S2. XPS analysis of the Ru_{fcc}/KB, Ru_{hcp}/KB, and $Ru_{fcc+hcp}$/KB.

Figure S3

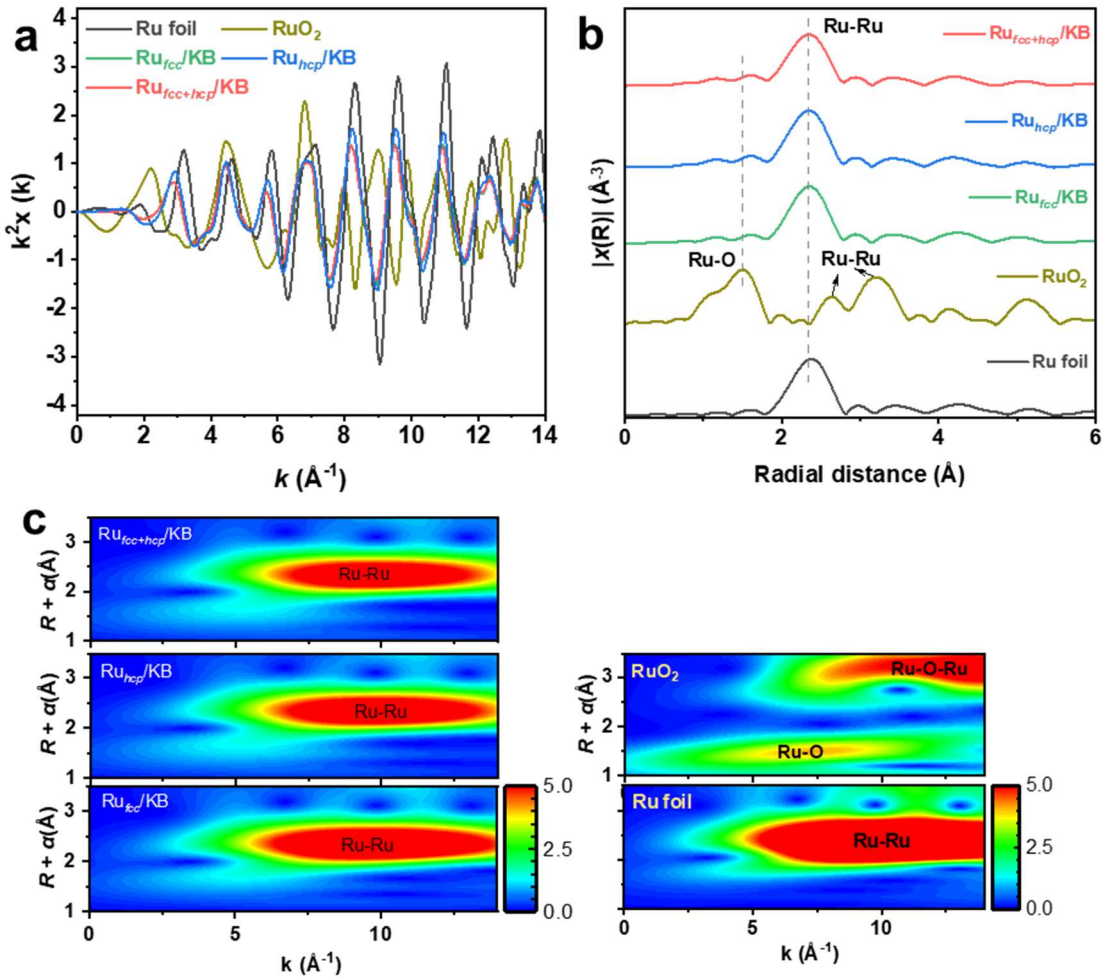

Figure S3. a) Experimental k^2-weighted EXAFS oscillations and **b)** extended XAFS spectra at Ru k-edge for Ru foil, RuO_2, Ru_{fcc}/KB, Ru_{hcp}/KB, and $Ru_{fcc+hcp}$/KB samples. **c)** WT for the EXAFS signals of Ru foil, RuO_2, Ru_{fcc}/KB, Ru_{hcp}/KB, and $Ru_{fcc+hcp}$/KB samples.

Figure S4

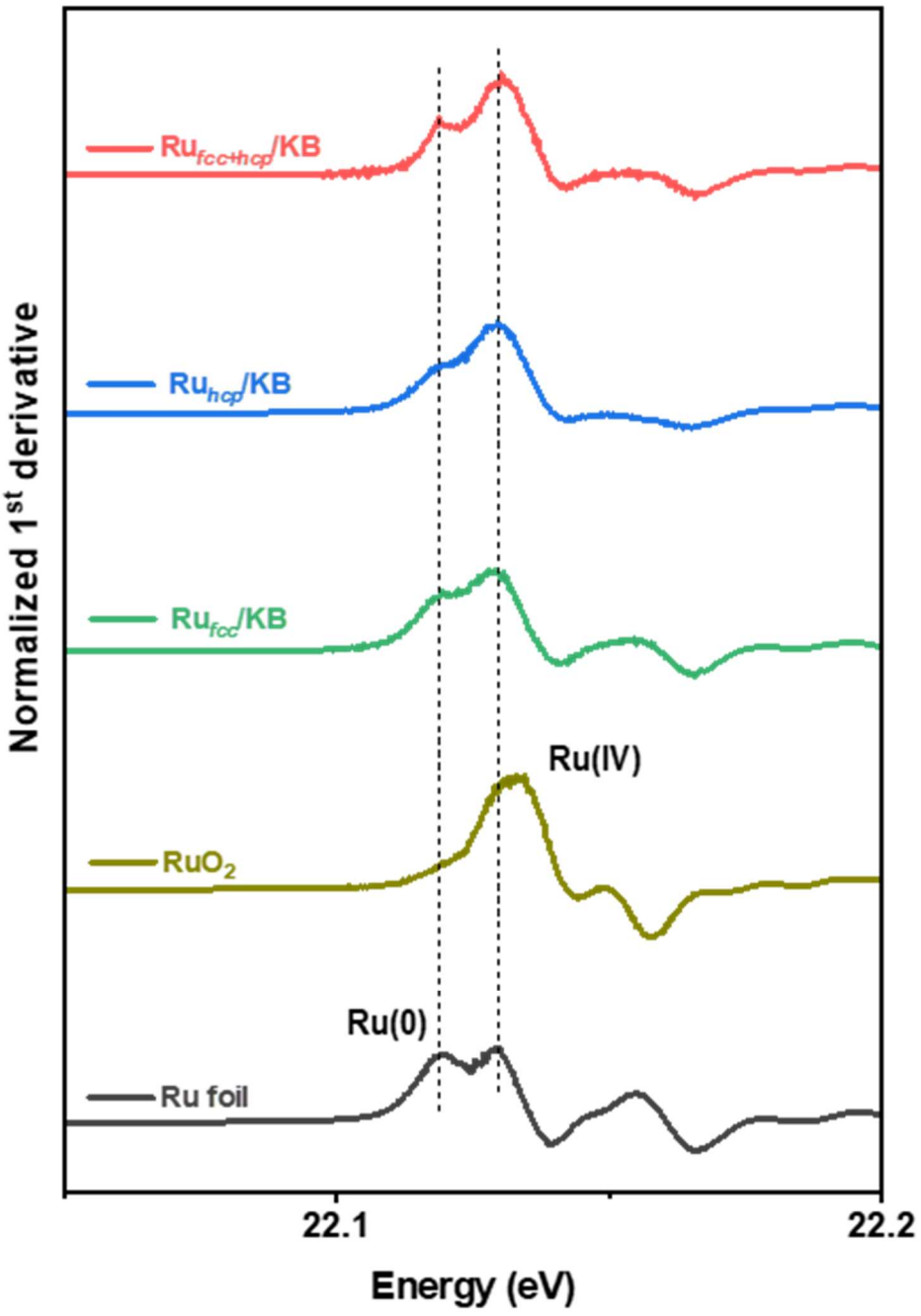

Figure S4. The corresponding first-order derivatives of the XANES spectra for Ru foil, RuO_2, Ru_{fcc}/KB, Ru_{hcp}/KB, and $Ru_{fcc+hcp}$/KB sample in Figure 2a.

Figure S5

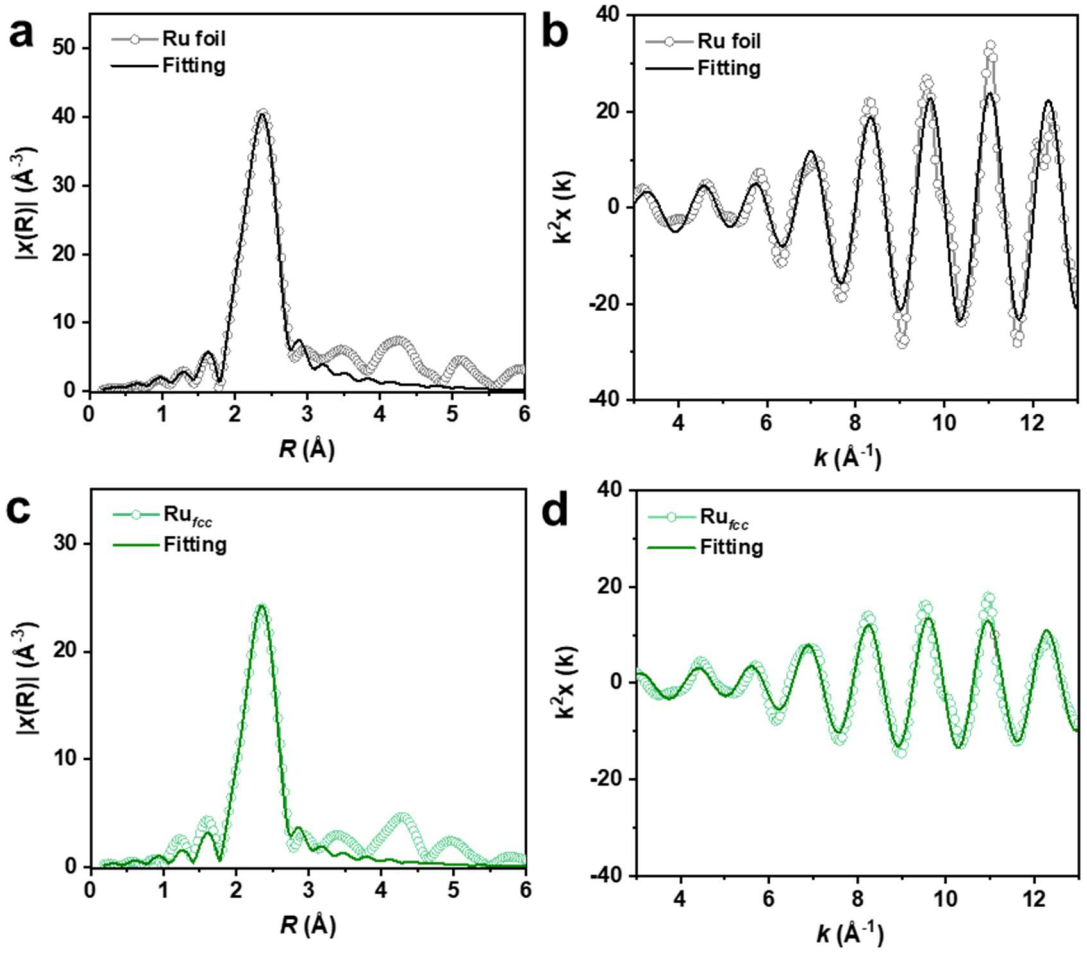

Figure S5. a-d) Fitted EXAFS data in R and K space of Ru K-edge; the detailed fitting information can be found in **Table S2**.

Figure S6

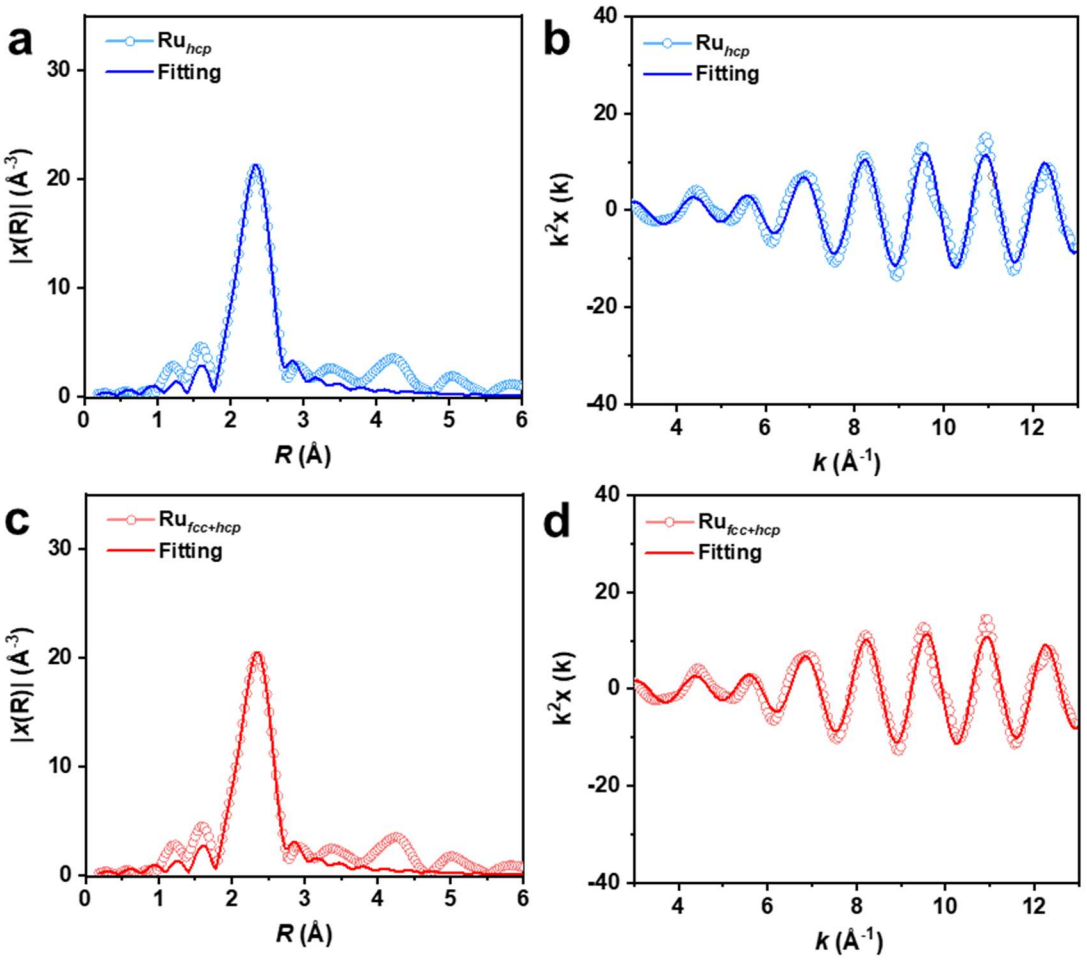

Figure S6. a-d) Fitted EXAFS data in R and K space of Ru K-edge; the detailed fitting information can be found in **Table S2**.

Figure S7

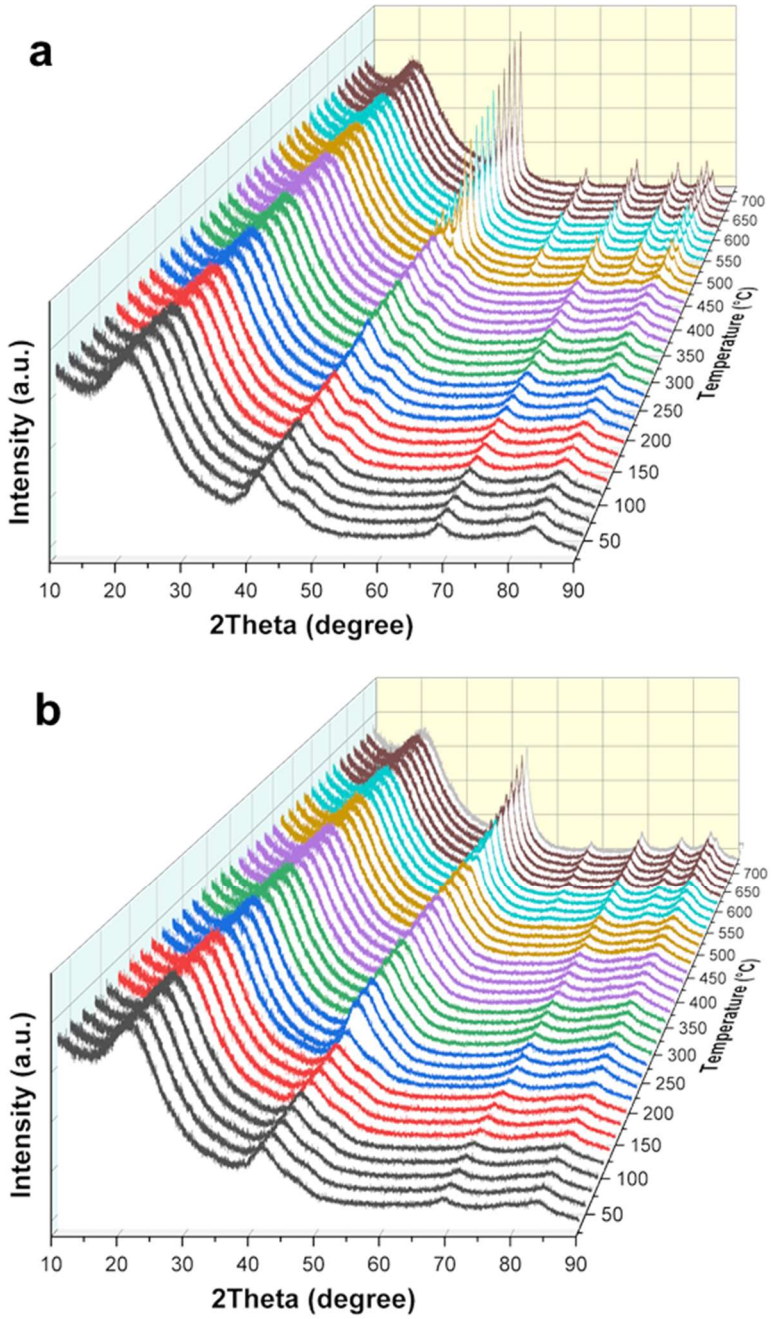

Figure S7. *In situ* XRD patterns of **a)** Ru_{fcc}/KB and **b)** $Ru_{hcp+fcc}$/KB under Ar in the temperature range between 30-690 ℃.

Both materials were subjected to heat under an Ar atmosphere, starting from 30 ℃ with a heating rate of 20 ℃ per minute. The characteristic peaks of *fcc*-Ru and *hcp*-Ru are marked by green and blue dashed lines, respectively. Green dashed lines: PDF#80-2333 (*fcc*-Ru). Blue dashed lines: PDF#70-0274 (*hcp*-Ru).

Figure S8

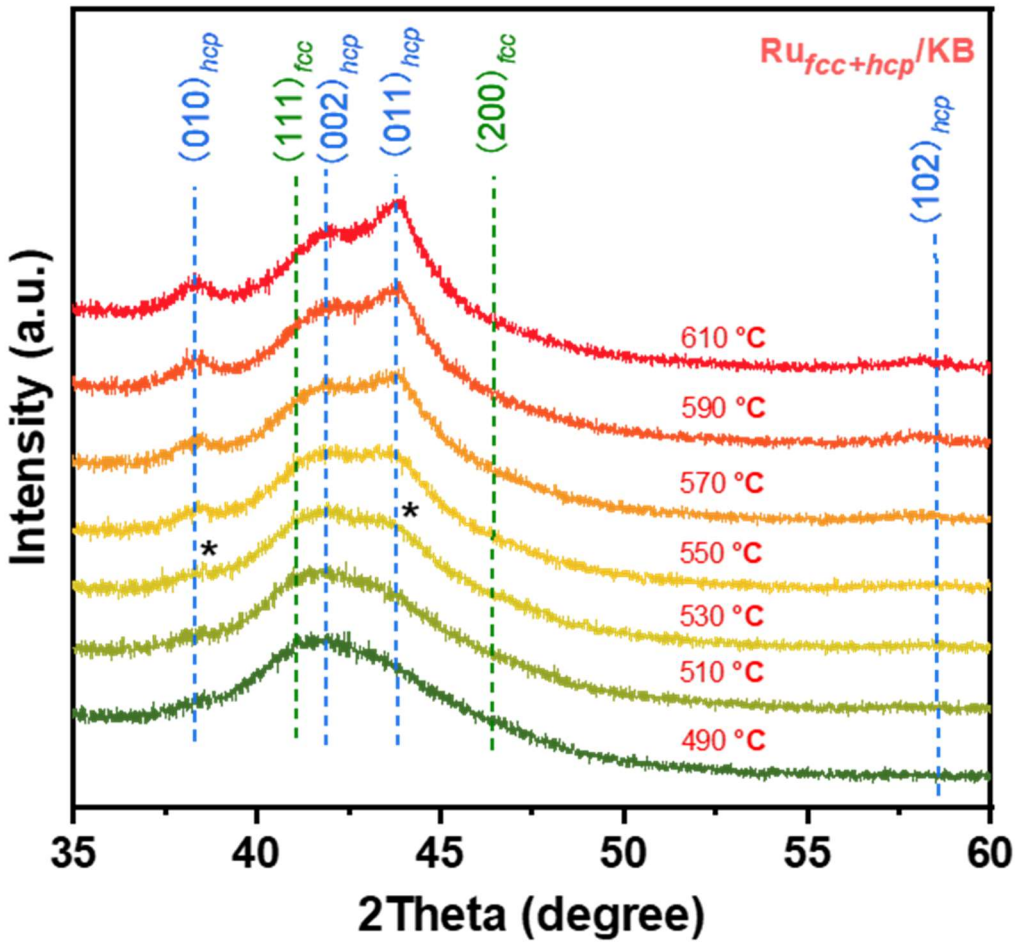

Figure S8. *In situ* XRD patterns of $Ru_{hcp+fcc}$/KB under Ar in the temperature range between 490-610 ℃.

Both materials were subjected to heat under an Ar atmosphere, starting from 30 ℃ with a heating rate of 20 ℃ per minute. The characteristic peaks of *fcc*-Ru and *hcp*-Ru are marked by green and blue dashed lines, respectively. Green dashed lines: PDF#80-2333 (*fcc*-Ru). Blue dashed lines: PDF#70-0274 (*hcp*-Ru).

Figure S9

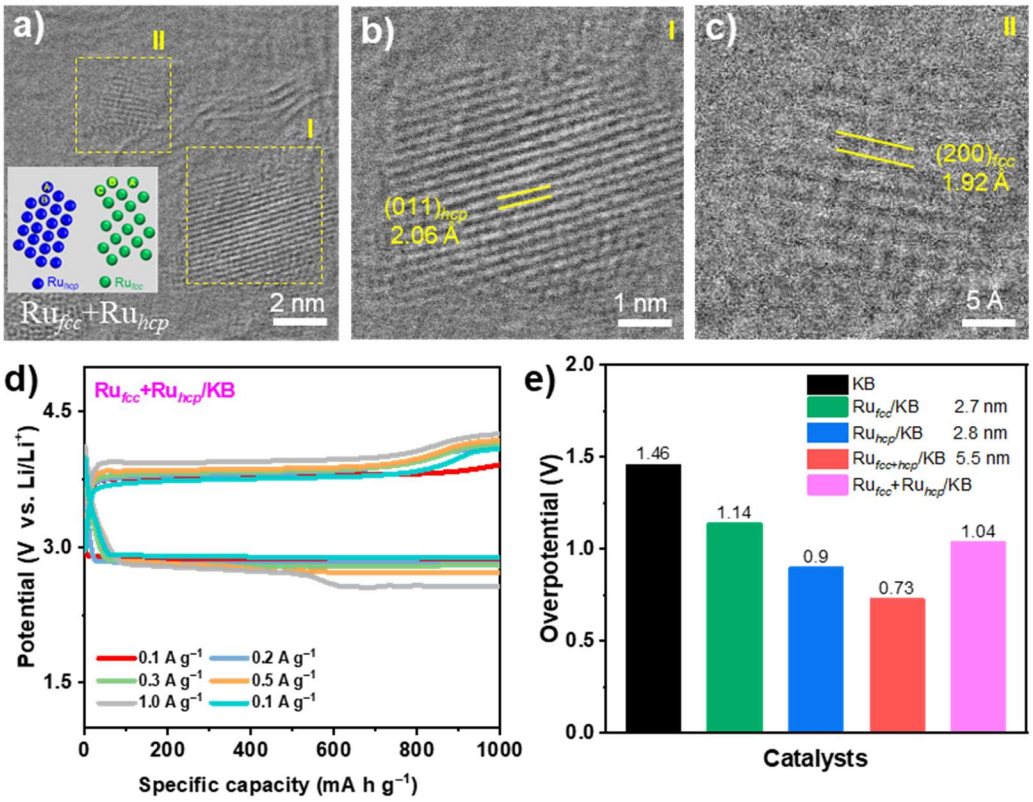

Figure S9. a-c) Atomically resolved HAADF-STEM image of of the Ru_{fcc}+Ru_{hcp}/KB. **d)** Charge and discharge curves of Ru_{fcc}+Ru_{hcp}/KB at different current densities. **e)** Overpotentials of different crystal phases Ru_{fcc}/KB, Ru_{hcp}/KB, $Ru_{fcc+hcp}$/KB and Ru_{fcc}+Ru_{hcp}/KB at current densities of 100 mA g^{-1} within a limiting capacity of 1000 mAh g^{-1}.

To investigate the effects of simultaneously loading two types of crystalline particles onto a carbon material without forming a heterophase interface, we attempted a one-pot wet-chemical method. This involved mixing KB, EG and TEG with $RuCl_3 \cdot xH_2O$, $Ru(acac)_3$, and PVP (the quantities of the aforementioned chemicals are listed in Table S1) to synthesize Ru_{fcc}+Ru_{hcp}/KB and evaluated its rate performance. The HAADF-STEM image of individual Ru_{fcc} and Ru_{hcp} particles, without interfacial formation, reveals lattice spacings of 2.06 Å and 1.92 Å, corresponding to the (011) facet of the hcp phase and the (200) facet of the fcc phase, respectively (Figure S9a-c). The results showed an overpotential of 1.04 V for Ru_{fcc}+Ru_{hcp}/KB catalyst (Figure S9e), which is higher than that of $Ru_{fcc+hcp}$/KB (0.73 V). This mixture does not generate a heterophase interface, which explains why its performance does not surpass that of the Ru heterophase materials.

Figure S10

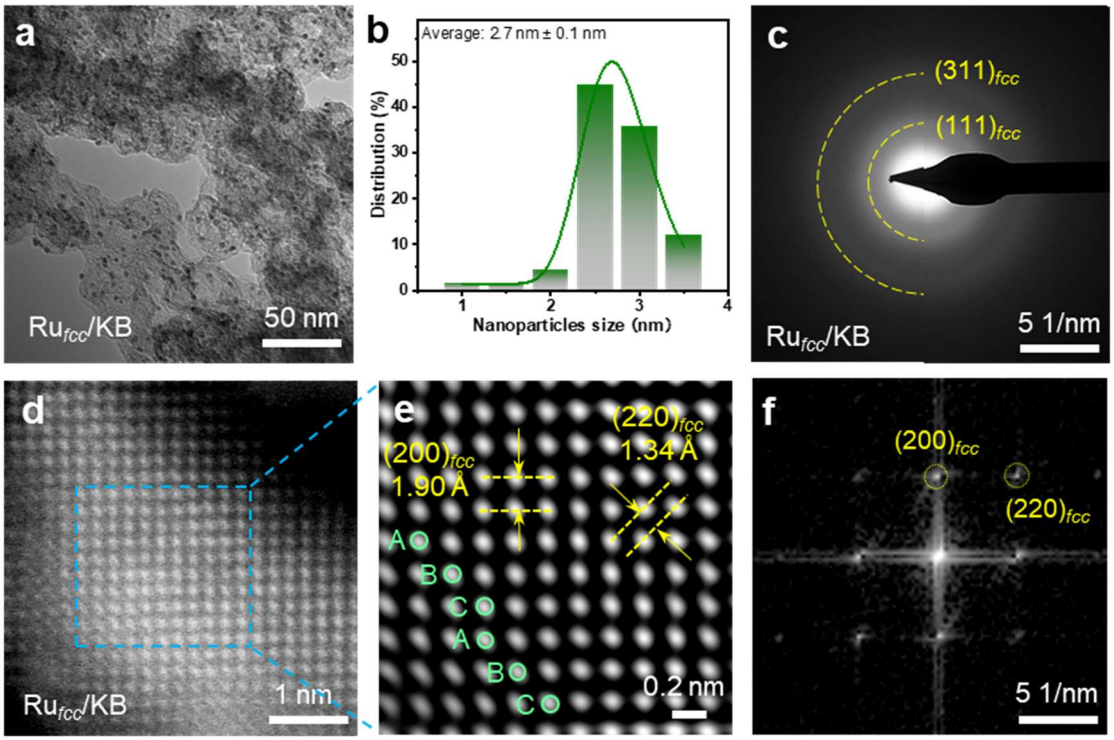

Figure S10. a) Representative HAADF-STEM image of the Ru$_{fcc}$/KB catalyst. **b)** Size distribution histogram (counted number of particles, 100). **c)** Selected-Area Electron Diffraction (SAED) pattern. **d)** Atomically resolved HAADF-STEM image of a Ru$_{fcc}$ particle. **e)** Simulated crystal structure image of the selected region in d). **f)** Fast Fourier transformation (FFT) pattern of a full region in images e).

Figure S11

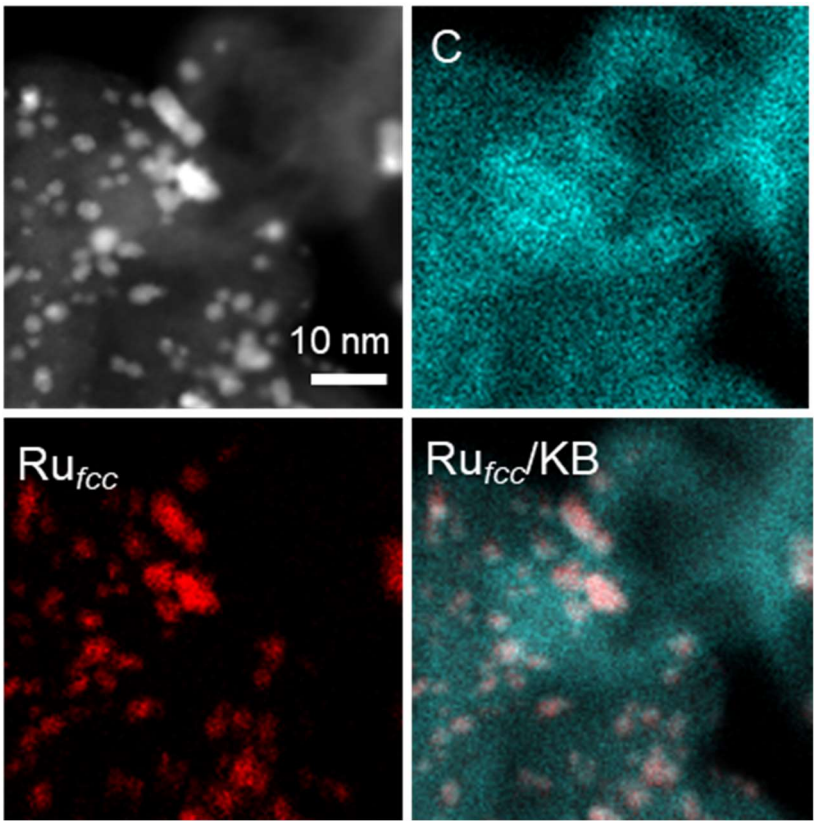

Figure S11. HAADF-STEM image of the chosen area of Ru$_{fcc}$/KB with corresponding elemental mapping.

Figure S12

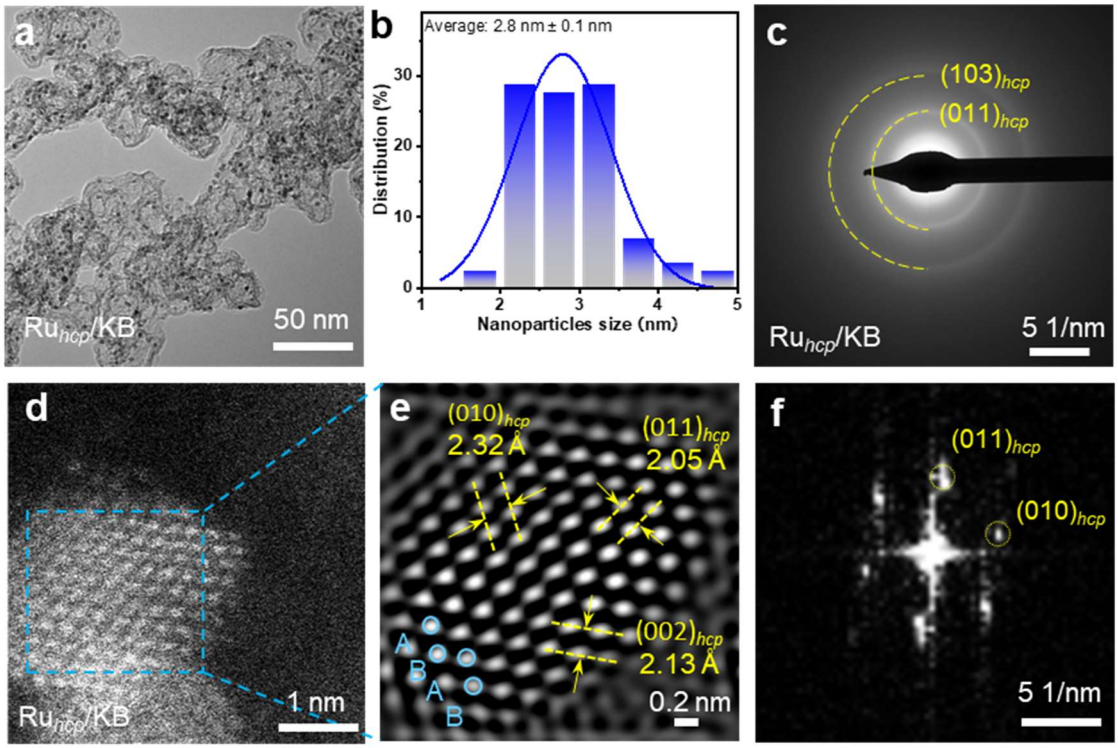

Figure S12. a) Representative HAADF-STEM image of the Ru$_{hcp}$/KB catalyst. **c)** Size distribution histogram (counted number of particles, 100). **c)** Selected-Area Electron Diffraction (SAED) pattern. **d)** Atomically resolved HAADF-STEM image of a Ru$_{hcp}$ particle. **e)** Simulated crystal structure image of the selected region in d). **f)** FFT image of a full region in images e).

Figure S13

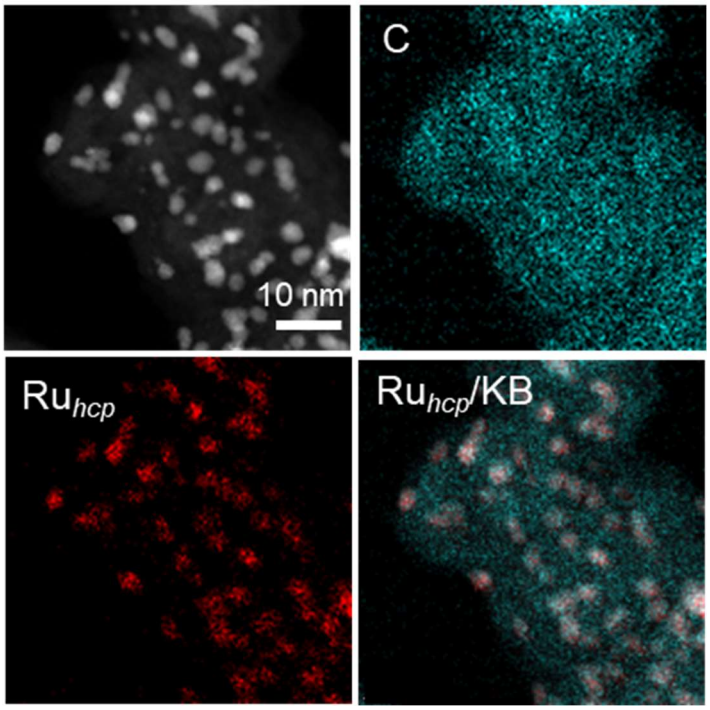

Figure S13. HAADF-STEM image of the chosen area of Ru$_{hcp}$/KB with corresponding elemental mapping.

Figure S14

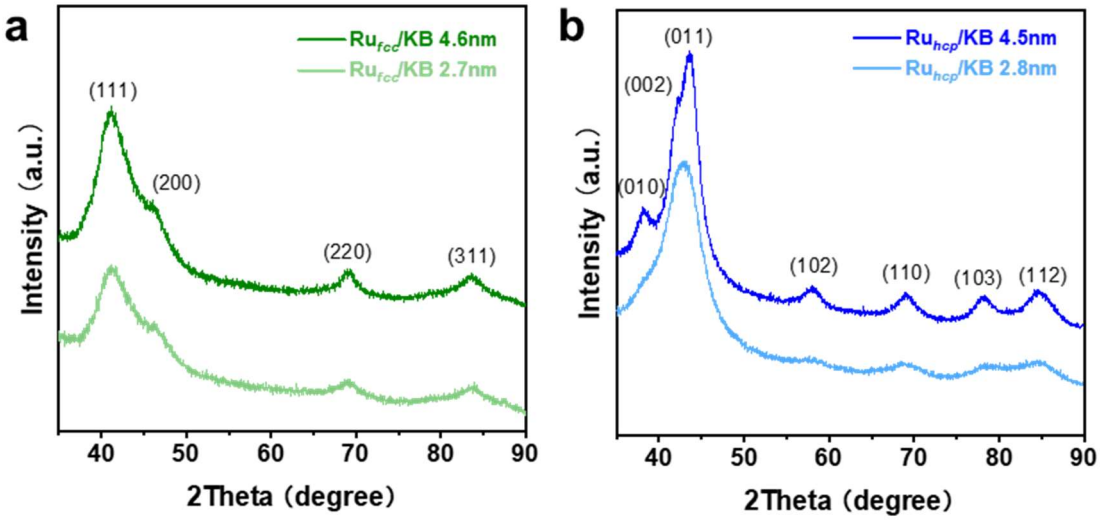

Figure S14. XRD pattern of **a)** Ru$_{fcc}$/KB and **b)** Ru$_{hcp}$/KB with different diameters.

We also synthesized Ru$_{fcc}$/KB and Ru$_{hcp}$/KB with sizes of approximately 3 and 5 nm. It was observed that the Ru NPs exhibit diffraction lines corresponding to the *fcc* and *hcp* structure in XRD patterns. The XRD peaks, including (111), (200), (220), and (311), align well with the standard *fcc* ruthenium patterns (JCPDS No. 80-2333). The XRD peaks, including (011), (102), (110), (103), and (112), align well with the standard *hcp* ruthenium patterns (JCPDS No. 70-0274).

Figure S15

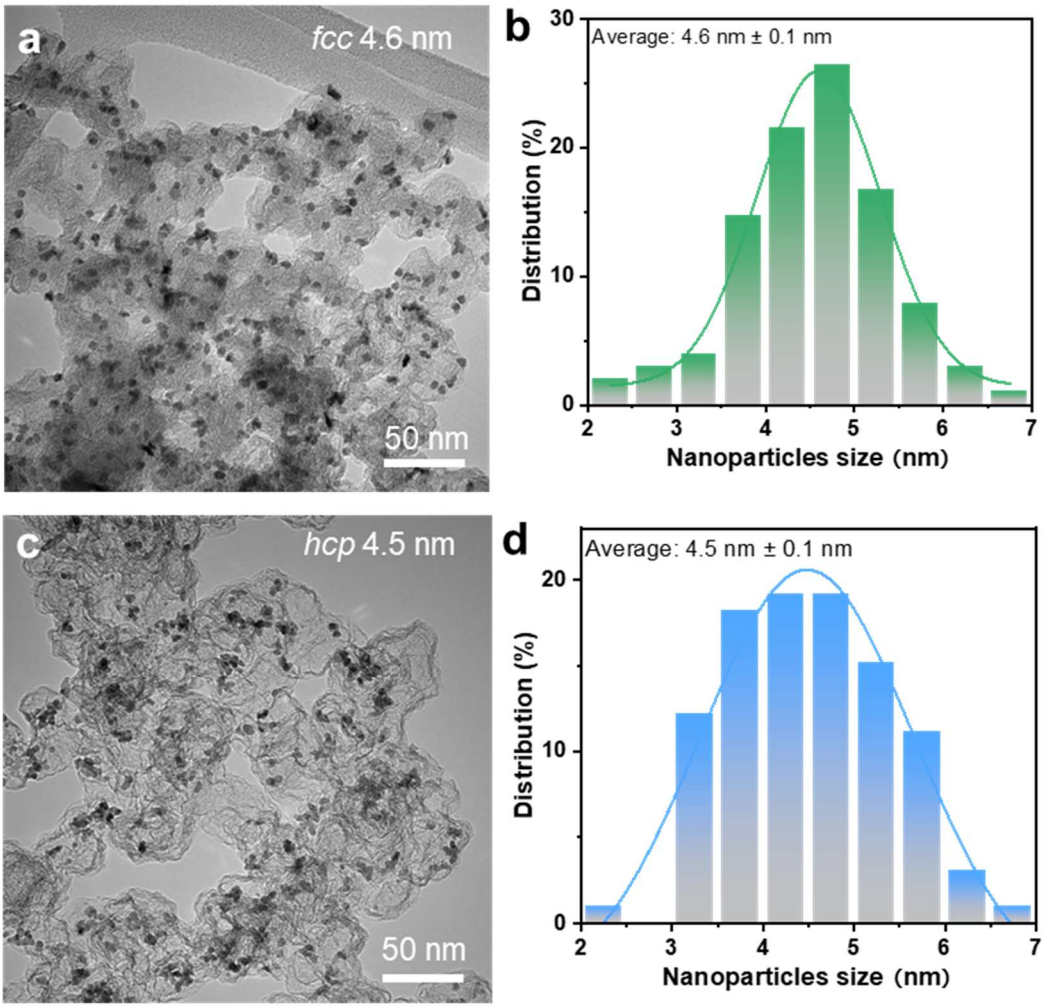

Figure S15. a,b) TEM and size distribution histogram of Ru_{fcc}/KB with diameters of ~5nm. **c,d)** TEM and size distribution histogram of Ru_{hcp}/KB with diameters of ~5nm.

We also synthesized Ru_{fcc}/KB and Ru_{hcp}/KB with sizes of approximately 5 nm. TEM images reveal that Ru nanopaticles had relatively comparable size distributions, measuring 4.6 nm for Ru_{fcc} and 4.5 nm for Ru_{hcp}.

Figure S16

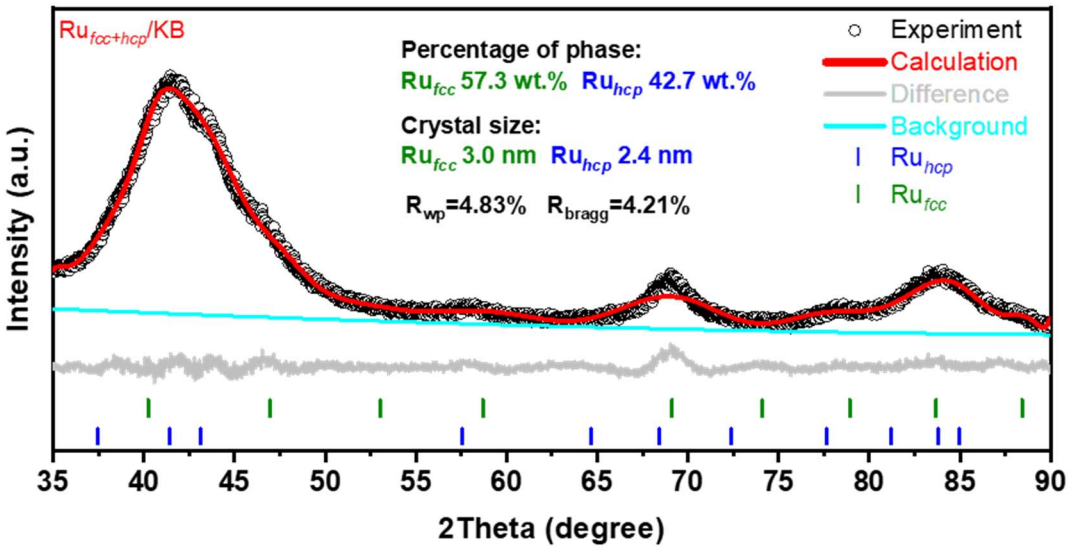

Figure S16. Rietveld refinement analysis of the Ru$_{fcc+hcp}$/KB. The tested XRD patterns are shown as black circles. The red curve is the calculated patterns for Ru$_{fcc+hcp}$/KB. The difference and background profiles are gray and cyanine curves, respectively.

Figure S17

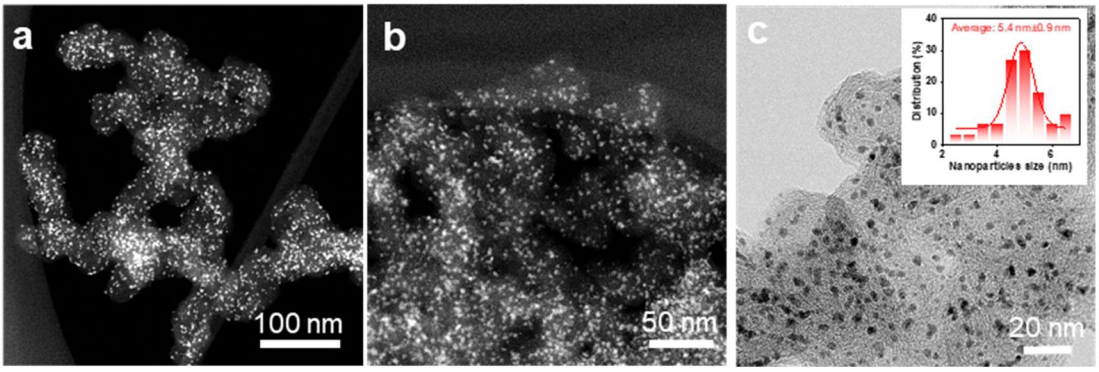

Figure S17. Representative **a,b)** dark-field and **c)** bright-field TEM images of the $Ru_{fcc+hcp}$/KB catalyst.

Figure S18

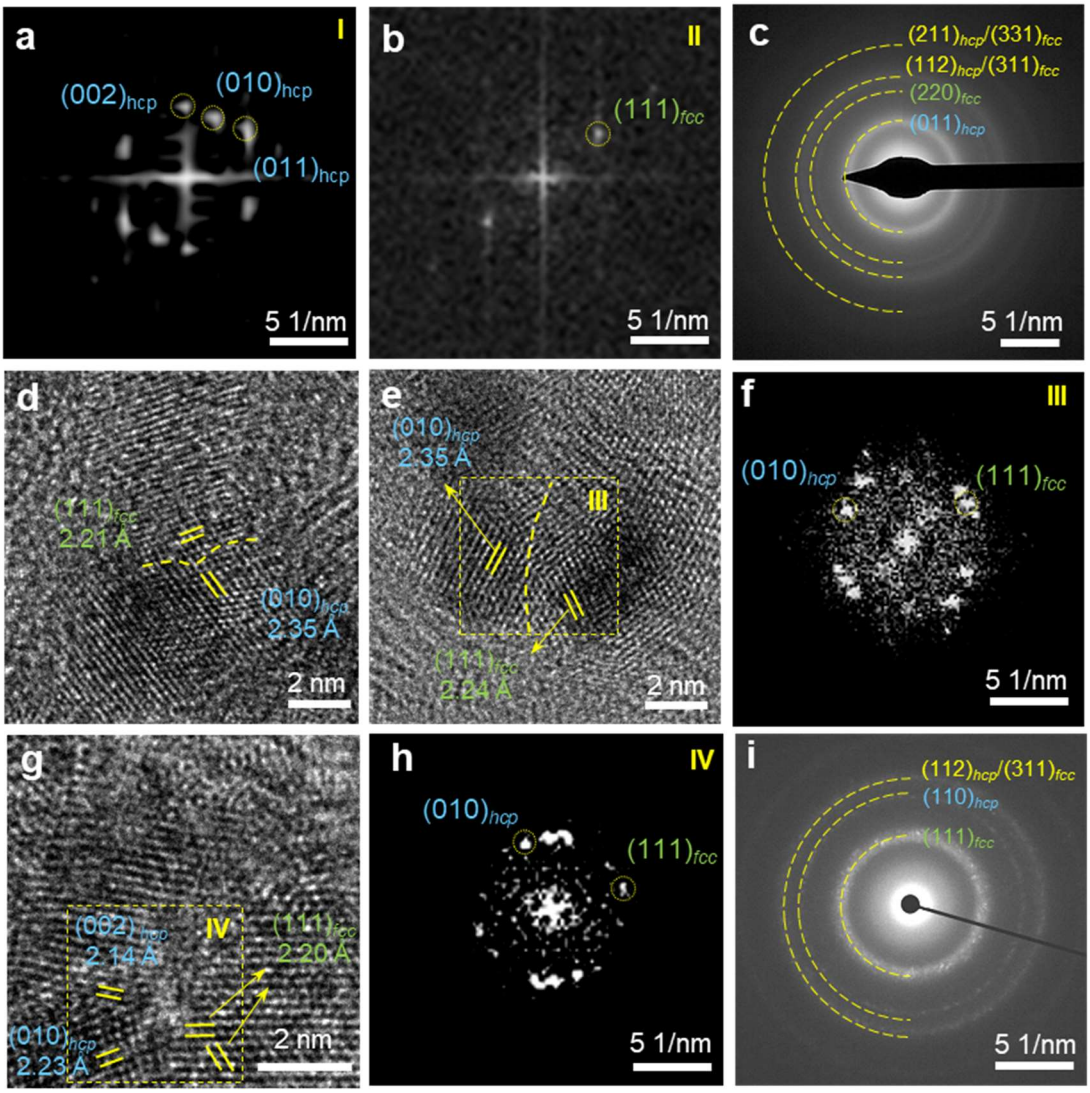

Figure S18. a,b) Fast Fourier transform (FFT) image and **c**) selected-area electron diffraction (SAED) pattern of Figure 1d. **d,e,g)** Representative HAADF-STEM image of the $Ru_{fcc+hcp}$/KB catalyst. **f)** FFT image of e). **h)** FFT image of g). **i)** Selected-area electron diffraction (SAED) pattern.

The HAADF-STEM image (Figure S18d, S18e and S18g) of individual $Ru_{fcc+hcp}$ particles reveals lattice spacings of around 2.21 Å and 2.35 Å, corresponding to the (111) of Ru_{fcc} phase and (010) facets of Ru_{hcp} phase, respectively. Besides, the *fcc* and *hcp* structure can be further confirmed by the corresponding FFT patterns in Figure S18f and S18h. The SAED patterns (Figure S18c and S18i) taken on samples show clear distinct rings corresponding to different planes of Ru_{fcc} and Ru_{hcp} structures, which indicate the formation of $Ru_{fcc+hcp}$ particles.

Figure S19

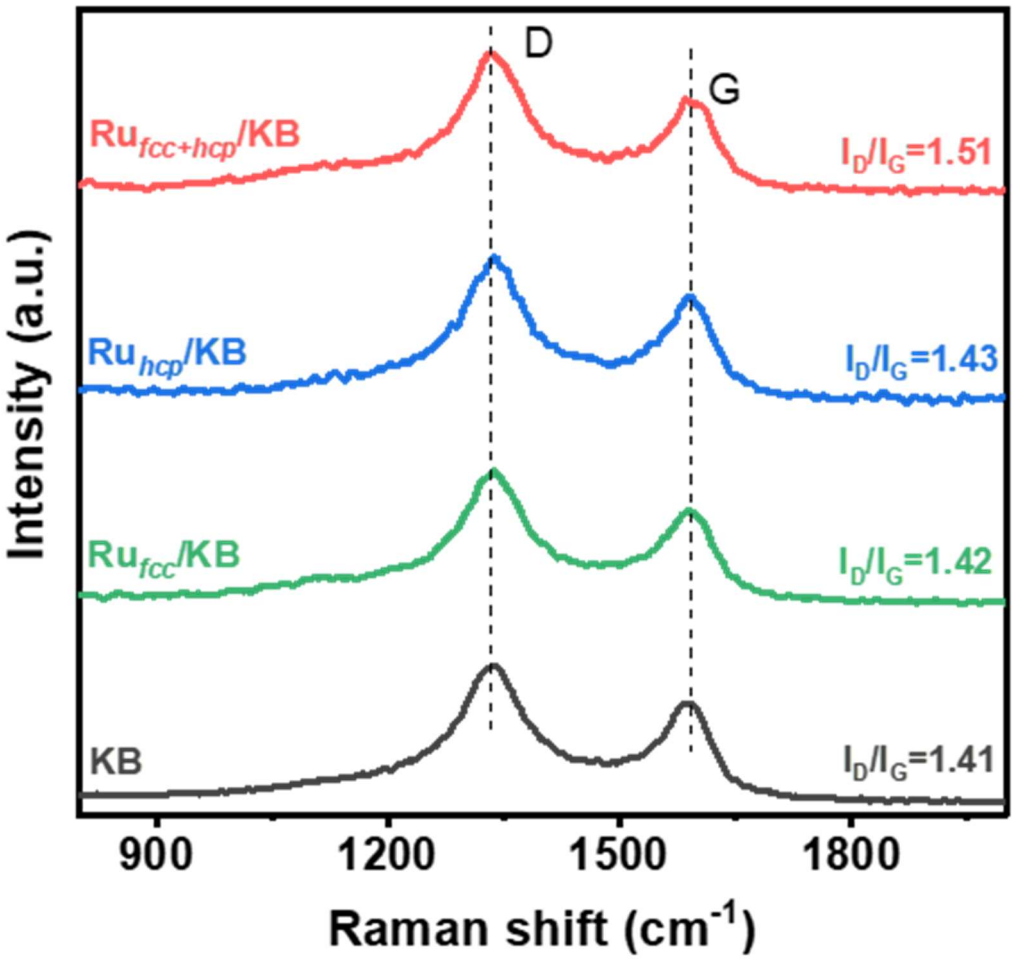

Figure S19. Raman spectra of pristine KB, Ru$_{fcc}$/KB (2.7 nm), Ru$_{hcp}$/KB (2.8 nm), Ru$_{fcc+hcp}$/KB (5.5 nm) materials.

Figure S20

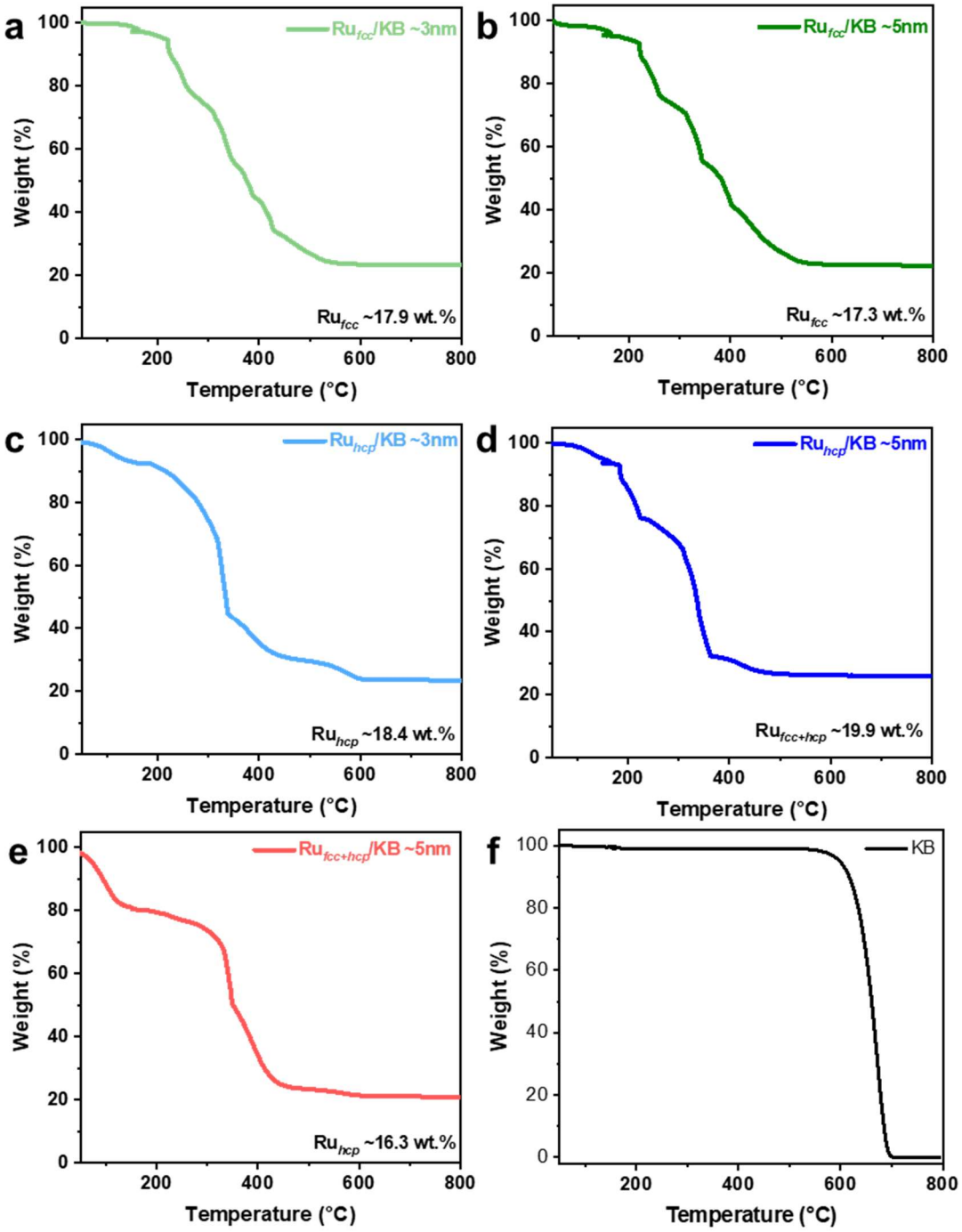

Figure S20. TGA analysis of the **a,b)** Ru$_{fcc}$/KB, **c,d)** Ru$_{hcp}$/KB, **e**) Ru$_{fcc+hcp}$/KB, and **f**) KB.

Assuming complete combustion of carbon and the conversion reaction of Ru to metal oxides (Ru_2O), the content of Ru in the Ru/KB catalysts can be determined using the following equation (1).

$$m_{Ru}\ (wt.\%) = \frac{m_{Ru}}{m_{\mathrm{Ru2O}}} \times \frac{Final\ weight}{Initial\ weight} \times 100\% \qquad \text{(Equ.1)}$$

Figure S21

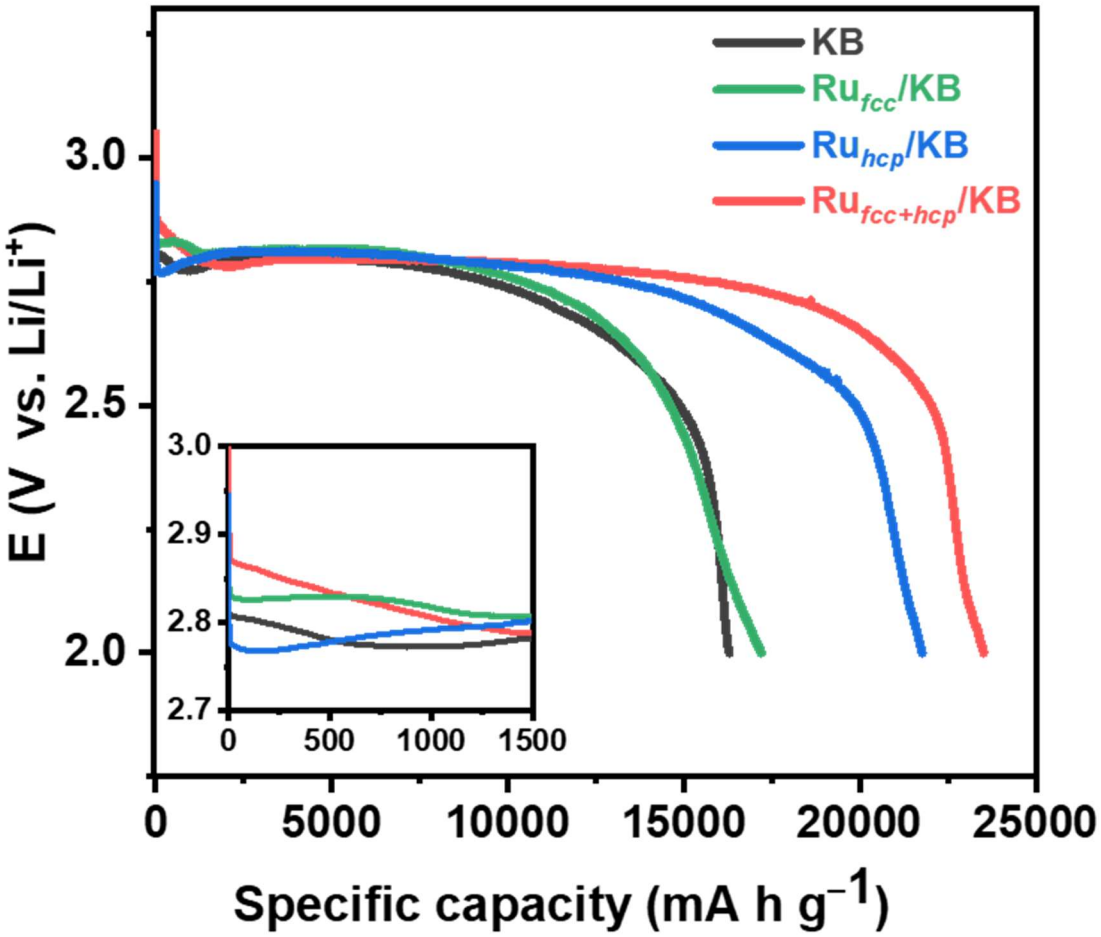

Figure S21. Full discharge curves of KB, Ru$_{fcc}$/KB, Ru$_{hcp}$/KB, and Ru$_{fcc+hcp}$/KB at 100 mA g^{-1}.

Figure S22

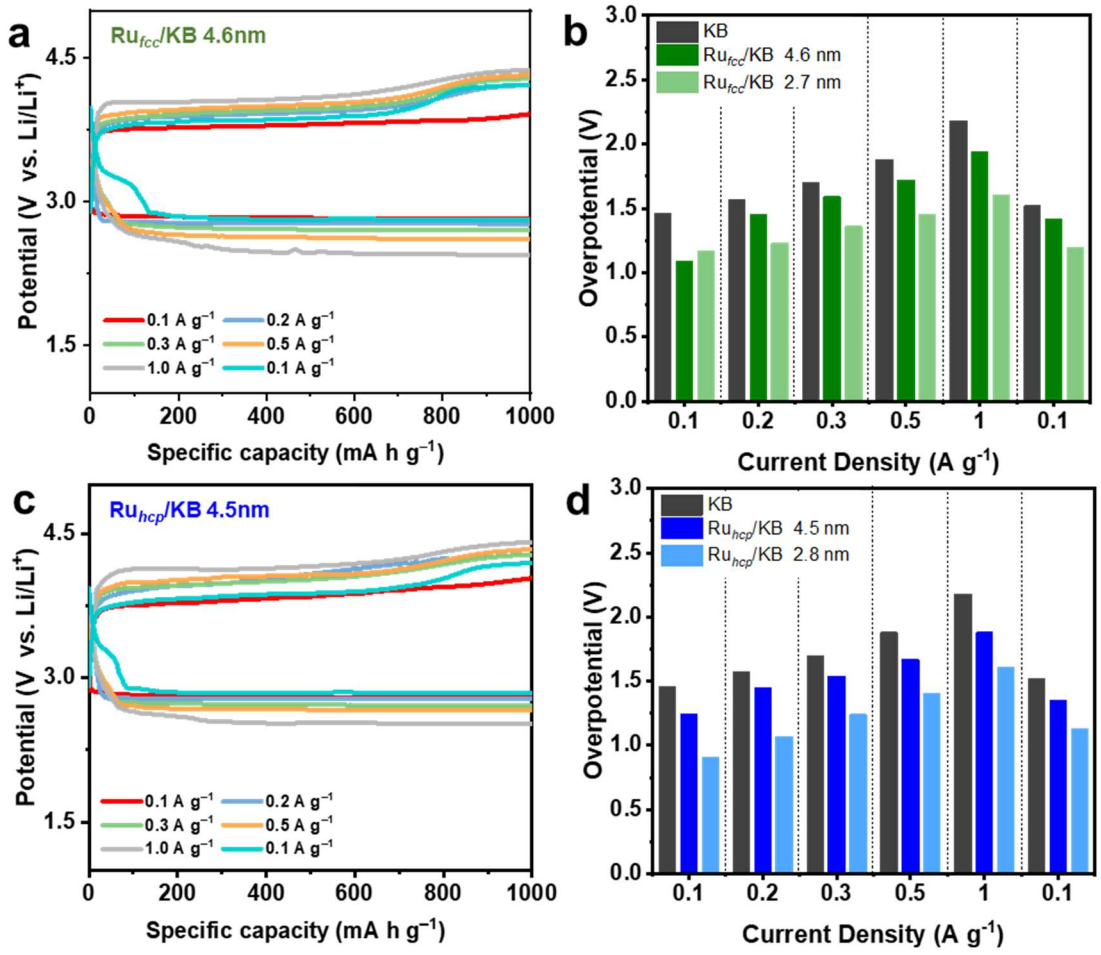

Figure S22. a) Charge and discharge curves of Ru$_{fcc}$/KB in 4.6 nm at different current densities. **b)** Battery overpotentials at various current densities of Ru$_{fcc}$/KB. **c)** Charge and discharge curves of Ru$_{hcp}$/KB in 4.5 nm at different current densities. **d)** Battery overpotentials at various current densities of Ru$_{hcp}$/KB.

Figure S23

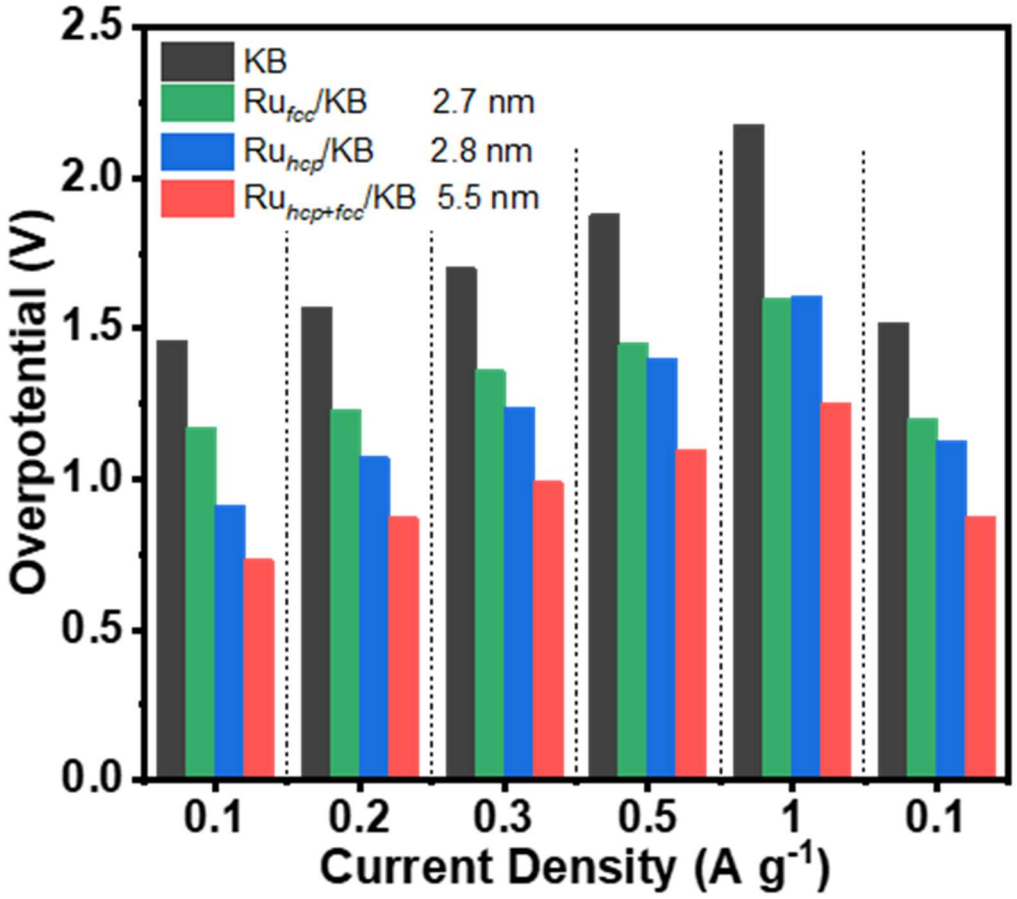

Figure S23. Overpotentials at various current densities of Ru_{fcc}/KB, Ru_{hcp}/KB, and $Ru_{fcc+hcp}$/KB within a limiting capacity of 1000 mAh g^{-1}.

Figure S24

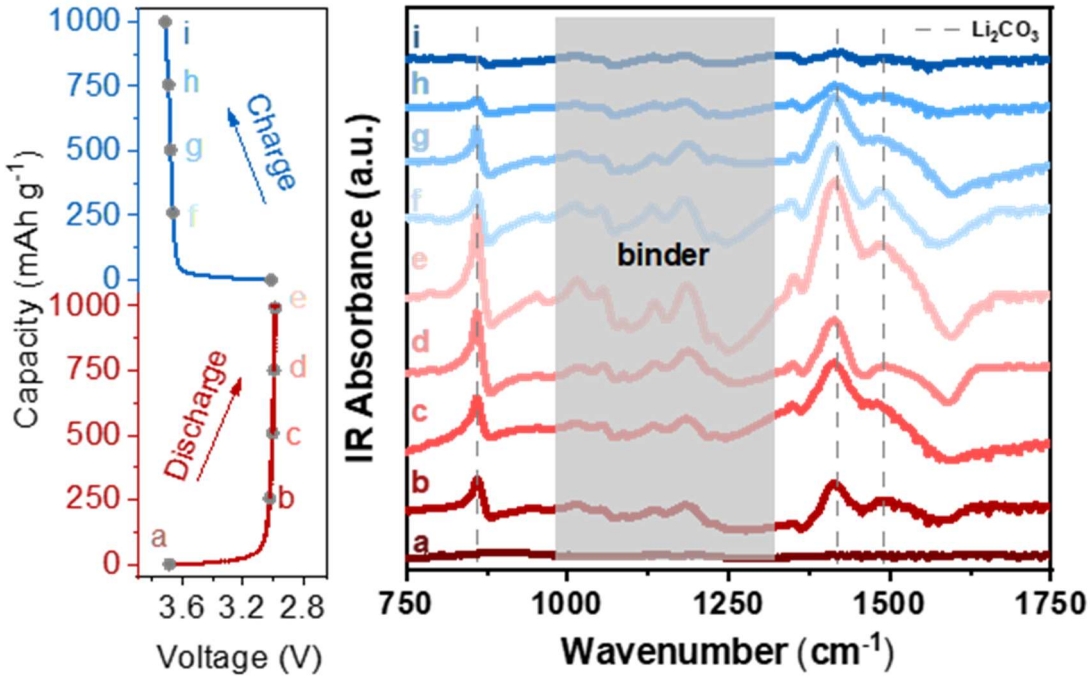

Figure S24. *Ex situ* FTIR spectra of $Ru_{hcp+fcc}$/KB cathodes during the first cycle at current densities of 100 mA g^{-1} within a limiting capacity of 1000 mAh g^{-1}.

Figure S25

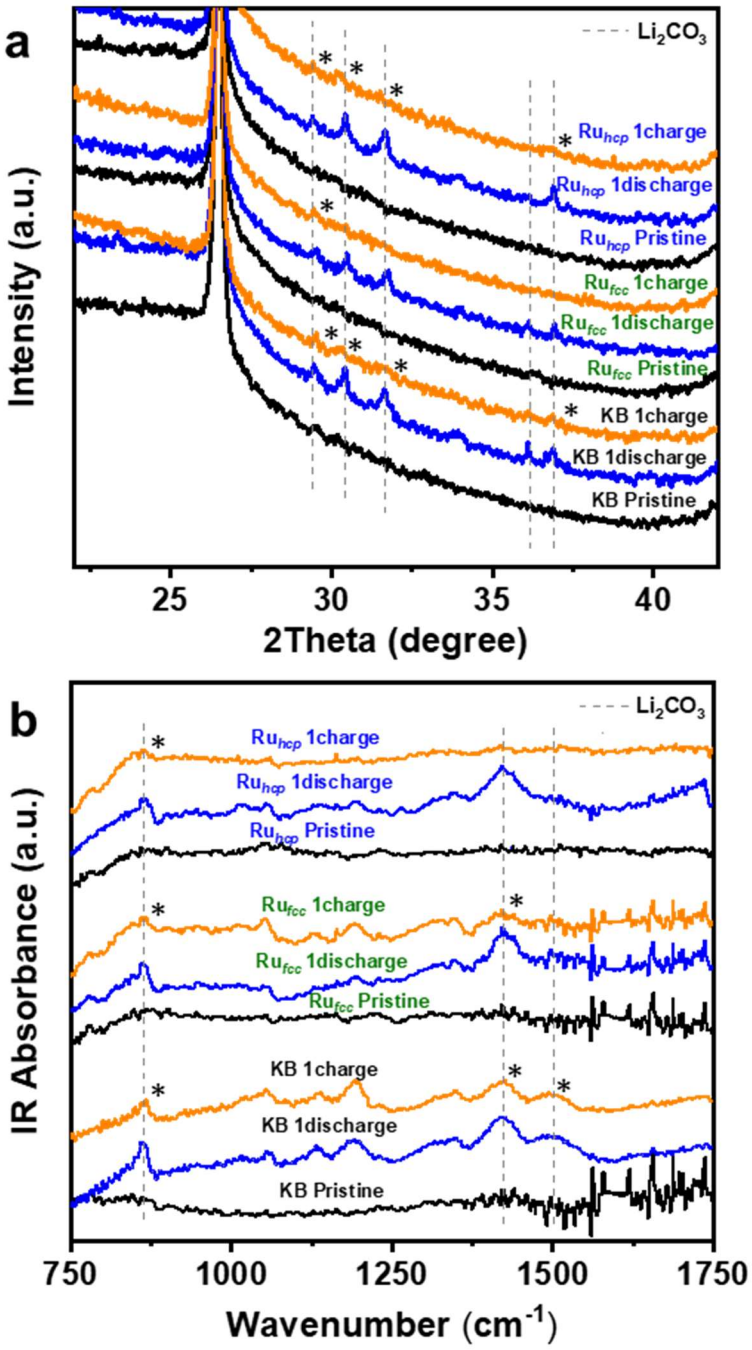

Figure S25. a) Ex situ XRD of KB, Ru_{fcc}/KB, and Ru_{hcp}/KB cathodes during the first cycle. and **b**) Ex situ FTIR spectra of KB, Ru_{fcc}/KB, and Ru_{hcp}/KB cathodes during the first cycle at current densities of 100 mA g^{-1} within a limiting capacity of 1000 mAh g^{-1}.

Figure S26

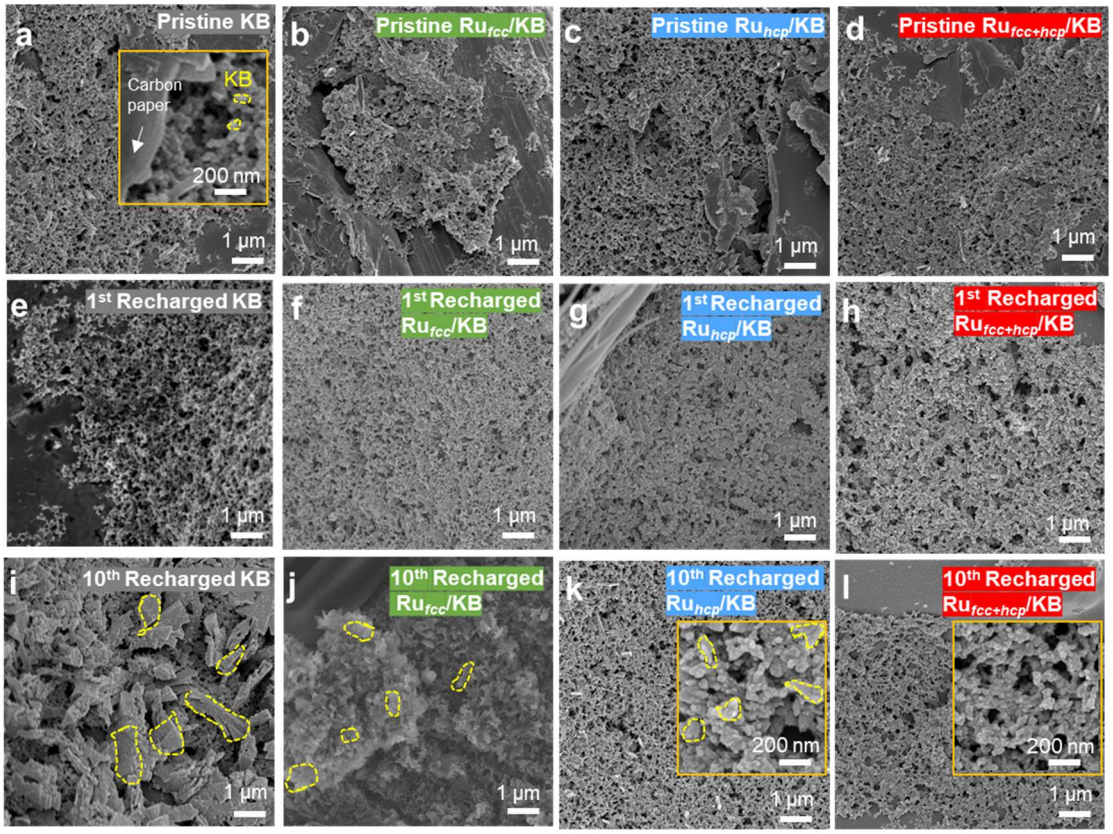

Figure S26. Typical SEM images of **a-d)** pristine and after **e-h)** first/ **i-l)** tenth recharged KB, Ru$_{fcc}$/KB, Ru$_{hcp}$/KB, and Ru$_{fcc+hcp}$/KB cathodes.

Figure S26a-d shows that pristine KB and the three Ru-based catalysts exhibit uniform particle sizes ranging from 50 to 100 nm (Figure S26a), with minimal agglomeration. The SEM images (Figure S26e-h) of these four materials after first recharge display similar morphologies to their pristine forms, indicating that the discharge products are nearly decomposed across the KB, Ru$_{hcp}$/KB, Ru$_{fcc}$/KB, and Ru$_{fcc+hcp}$/KB catalysts after the first recharge cycle. This suggests comparable levels of residual discharge products among them. To further understand the long-term behavior of discharge product decomposition, we extended our SEM analysis to cathodes after ten cycles at a current density of 100 mA g^{-1} with a limiting capacity of 1000 mAh g^{-1}. As shown in Figure S26i-l, the Ru$_{fcc+hcp}$/KB cathode exhibits a surface morphology similar to the initial state, suggesting that the discharge products were nearly fully decomposed after ten repeated cycling. In contrast, different from the morphologies observed in its initial status, noticeable residual discharge products (outlined by yellow area) are observed in the KB, Ru$_{fcc}$/KB, and Ru$_{hcp}$/KB cathodes after ten cycles.

Figure S27

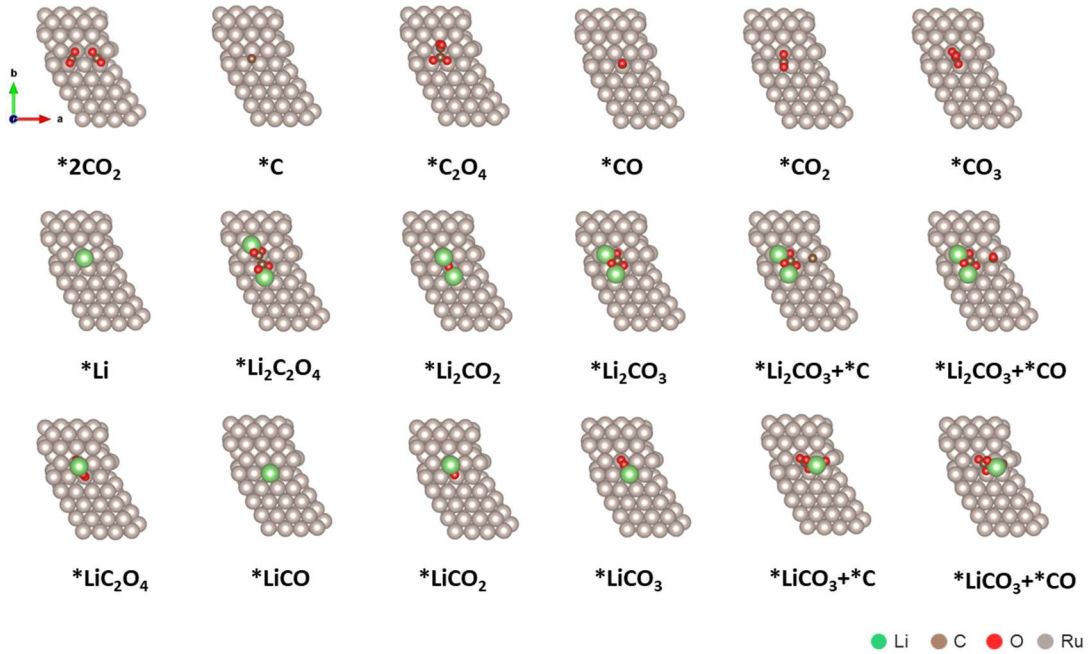

Figure S27. Structural modelling of reactants or intermediates at different sites of the $Ru_{fcc+hcp}$ cluster.

Figure S28

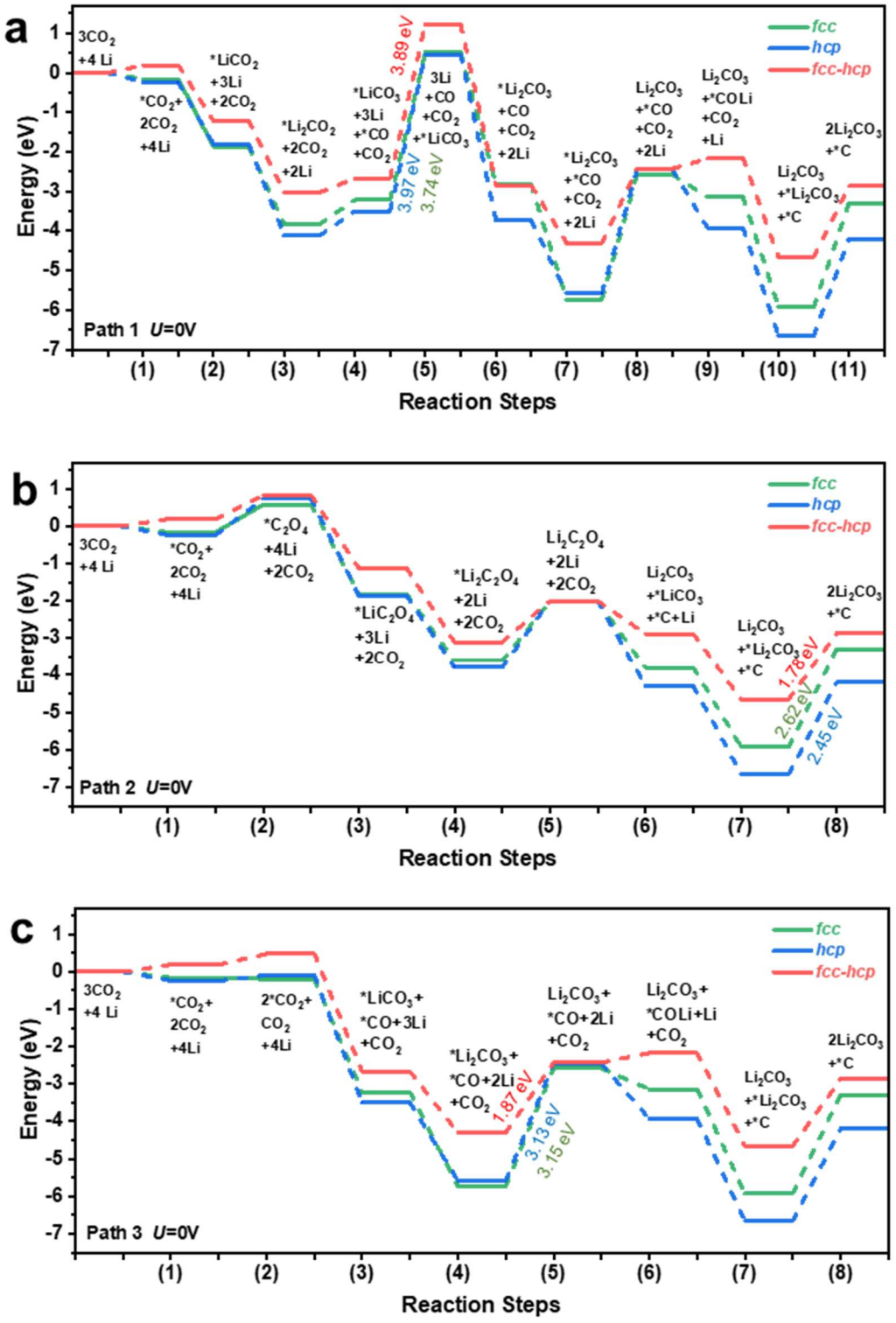

Figure S28. The free energy diagram of Ru-cluster under an applied potential U = 0 V.

Table S1. Reaction conditions for the synthesis of *fcc* and *hcp* Ru nanoparticles/KB materials.

No.	Catalysts	metal precursor/mmol	solvent/mL	mmol of PVP	Temperatue °C
1	Ru_{fcc}/KB-3nm	$Ru(acac)_3$/0.21	TEG/30	1.0	200
2	Ru_{fcc}/KB-5nm	$Ru(acac)_3$/0.21	TEG/10	0.5	200
3	Ru_{hcp}/KB-3nm	$RuCl_3 \cdot xH_2O$/0.21	EG/30	1.0	180
4	Ru_{hcp}/KB-5nm	$RuCl_3 \cdot xH_2O$/0.21	EG/10	0.5	180
5	$Ru_{fcc+hcp}$/KB-5nm	$Ru(acac)_3$/0.21	TEG/30	1.0	200
		$RuCl_3 \cdot xH_2O$/0.21	EG/30	1.0	180
6	Ru_{fcc} + Ru_{hcp}/KB	$RuCl_3 \cdot xH_2O$/0.21 $Ru(acac)_3$/0.21	TEG/30 EG/30	2.0	200

Table S2. EXAFS fitting results for different materials at Ru K-edge.

Materials	***pair***	***CN***	***R (Å)***	**σ^2 ($\times10^{-3}$Å^2)**	**ΔE_o(eV)**	**R-factor**
Ru foil	Ru-Ru	12.0	2.670	2.7±0.7	0.7±1.0	0.011
Ru_{fcc}	Ru-Ru	7.3±1.0	2.674	5.0±0.8	-4.8±1.1	0.017
Ru_{hcp}	Ru-Ru	6.2±1.0	2.674	4.8±0.9	-5.7±1.3	0.024
$Ru_{fcc+hcp}$	Ru-Ru	5.2±1.0	2.681	7.1±1.3	-12.0±1.5	0.027

CN - Coordination number

R - Interatomic distance

σ^2 - Debye-Waller factor (thermal and static disorder in absorber-scatterer distances)

ΔE_0 - Edge energy shift (the difference between the zero kinetic energy value of the sample and that of standard theoretical model)

R factor - Goodness of fitting

Table S3. Cycling performance of Ru-based catalysts as cathodes reported in recent literatures.

Cathodes	Overpotential V (current density mA g^{-1} /cut-off capacity mAh g^{-1})	Discharge capacity mAh g^{-1} (current density mA g^{-1})	Cycle stability hours (current density mA g^{-1} /cut-off capacity mAh g^{-1})	Electrolytes	Journal, Year
This work $Ru_{fcc+hcp}$/KB	0.73 (100/1000)	23517 (100)	2260 (100/1000)	1 M LiTFSI/DMSO	
SA Ru-Co_3O_4/CC[3]	1.05 (100/500)	30915 (100)	>2000 (200/800)	1 M LiTFSI/TEGDME	Adv. Sci., 2021
SA Ru_h-NC@rGO[4]	0.97 (100/1000)	44700 (100)	734 (1000/1000)	1 M LiTFSI/TEGDME	ACS Appl. Mater. Interfaces, 2022
Ru_{AC+SA}@NC[5]	1.05 (100/1000)	10651.9 (100)	≈230 (300/500)	1 M LiTFSI/TEGDME	Adv. Mater., 2022
Ru/Co-CPY@CNT-2[6]	0.84 (100/1000)	24740 (200)	720 (500/1000)	1 M LiTFSI/TEGDME	Cell Rep. Phys. Sci., 2021
RuCo NSs/CNT[7]	0.94 (100/1000)	8057 (100)	110 (250/500)	1 M LiTFSI/DMSO	Adv. Funct. Mater., 2022
Ru-O-Zr/Ce[8]	1.03 (100/1000)	21 075 (100)	3340 (100/1000)	1 M $LiCF_3SO_3$	Adv. Energy Mater., 2023
HOF-FJU-1-Ru@CNT[9]	1.09 (100/1000)	24245 (100)	1800 (400)	1 M LiTFSI/TEGDM	Angew. Chem. Int. Ed. Engl., 2023
RuNi/MWCNTs[10]	1.15 (200/500)	13608 (100)	400 (200/500)	1 M LiTFSI/DMSO	Chemsuschem., 2023
Ru/CNT[11]	1.24 (100/500)	4541 (100)	450 (100/500)	1 M LiTFSI/TEGDM	ACS Appl. Mater. Interfaces, 2021
Ru/CNTs[12]	0.95 (100/1000)	11888 (100)	2000 (100/1000)	1M LiTFSI/DMSO	ACS Energy Lett., 2024
Ru-GDYS[13]	1.67 (500/1000)	15030 (500)	480 (500/1000)	1 M LiTFSI/TEGDM	Chin. Chem. Lett., 2024
GNR/Ru[14]	1.34 (100/500)	11470 (100)	1240 (100/500)	1.5 M LiTFSI/0.45 M $LiNO_3$/ DMSO	J. Mater. Chem. A, 2024
MP-RuCoAl alloy ⊥ CoAl-LDH[15]	1.3 (200/1000)	-	2270 (200/1000)	0.5 M LiTFSI/TEGDME	Nano Res., 2024
MP-Cu_2O/RuAl[16]	1.43 (100/1000)	11677 (100)	1750 (200/1000)	0.5 M LiFSI/TEGDM	J. Energy Chem., 2024
Ru-AHCNs[17]	1.38 (100/1000)	11194.4 (100)	1000 (100/1000)	1 M LiTFSI/TEGDM	J. Power Sources, 2024
4H/fcc Ru−Ni[18]	0.65 (50/500)	17360.1 (50)	800 (250/500)	3 M LiTFSI/DMSO/25%vol. $EmimBF_4$	Angew. Chem., Int. Ed. Engl., 2024
$(H_2IMes)(Cl)_2(pyr)_2RuCHPh)$[19]	0.86 (100/500)	29 697.2 (300)	1267 (300/1000)	1 M LiTFSI/TEGDM	J. Am. Chem. Soc., 2024
KB/NP-RuAl/Ru[20]	1.18 (200/1000)	-	1400 (200/1000)	0.5 M LiTFSI/TEGDM	Nano Energy, 2023

Cathodes	Overpotential V (current density mA g^{-1} /cut-off capacity mAh g^{-1})	Discharge capacity mAh g^{-1} (current density mA g^{-1})	Cycle stability hours (current density mA g^{-1} /cut-off capacity mAh g^{-1})	Electrolytes	Journal, Year
Ru/Fe-TAPP@GO[21]	0.82 (100/1000)	39000 (100)	800 (300/1000)	1 M LiTFSI/TEGDM	Chin. Chem. Lett., 2023
IrRu/N-CNT[22]	~1 (100/500)	6228 (100)	7660 (100/500)	1 M LiTFSI/TEGDM	Adv. Funct. Mater., 2023
Ru/RuO_2-HPC[23]	1.22 (250/1000)	12398 (250)	2424 (250/1000)	1 M $LiCF_3SO_3$/TEGDME	ChemistrySelect, 2022
$Ru(acac)_3$ RM-CNT[24]	1.28 (200/1000)	6306 (200)	400 (100/1000)	1 M $LiCF_3SO_3$/TEGDM	Chem. Eng. J., 2022
Ni/Ru HNPs[25]	0.88 (200/1000)	~10000 (200)	1200 (200/1000)	1 M LiTFSI/TEGDM	Adv. Mater., 2022
$Ru(bpy)_3Cl_2$[26]	>1 (100/1000)	22119 (200)	400 (300/1000)	1 M LiTFSI/TEGDM	Angew. Chem., 2021
Ru@CNT[27]	1.39 (100/500)	23102 (100)	1000 (100/500)	LiTFSI/NaTFSI/ TEGDM	ACS Appl. Mater. Interfaces, 2021
RuRh/VC72[28]	1.35 (1000/1000)	9600 (200)	1900 (200/1000)	1 M LiTFSI/DMSO	Matter, 2020
RuO_2–TiO_2 NAs/CT[29]	1.05 (250/1000)	16727 (250)	1904 (250/1000)	1 M LiTFSI/TEGDM	J. Power Sources, 2020
Ru/NS-G[30]	1.13 (100/1000)	12448 (100)	2000 (100/1000)	1 M LiTFSI/TEGDM	Energy Stor. Mater., 2020
Ru/ACNFs[31]	1.35 (100/1000)	11495 (200)	1000 (100/1000)	1 M LiTFSI/TEGDM	Energy Environ. Sci., 2019
CNT@RuO_2[32]	1.36 (50/500)	2187 (50)	110 (50/500)	0.2M $LiCF_3SO_3$/ TEGDME	ACS Appl. Mater. Interfaces, 2019
Ru/Ni foam[33]	>1 (200/1000)	9502 (100)	2000 (200/1000)	1 M LiTFSI/TEGDM	Electrochim. Acta, 2019
RuP_2-NPCF[34]	1.3 (200/1000)	11951 (100)	2000 (200/1000)	1 M LiTFSI/TEGDM	Small, 2019
COF-Ru@CNT[35]	1.24 (200/1000)	27348 (200)	750 (400/1000)	1 M LiTFSI/TEGDM	Adv. Mater., 2019
Ru–Cu–G[36]	0.88 (200/1000)	13698 (200)	1000 (200/1000)	1 M LiTFSI/TEGDM	Adv. Energy Mater., 2019
RuCu/CNFs[37]	1.45 (1000/1000)	15753 (300)	440 (500/1000)	1M LiTFSI/DMSO	Chem. Eng. J., 2019
Ru@Super P[38]	1.71 (100/1000)	8229 (100)	1600 (100/1000)	0.2M $LiCF_3SO_3$/tetraglyme	Energy Environ. Sci., 2017

Table S4. The free energy change of each reaction step on the basal plane of Ru cluster and RU cluster (under an applied potential U = 0 V).

	Reaction	Step-by-step	Discharge energy barrier (eV)			Charge energy barrier (eV)		
			fcc	*hcp*	*fcc-hcp*	*fcc*	*hcp*	*fcc-hcp*
	Path 1							
(0)	$3CO_2 + 4Li$							
(1)	$*CO_2 + 2CO_2 + 4\ Li$	**(0) ⇌ (1)**	-0.16	-0.24	0.19	0.16	0.24	-0.19
(2)	$*LiCO_2 + 3Li + 2CO_2$	**(1) ⇌ (2)**	-1.72	-1.57	-1.41	1.72	1.57	1.41
(3)	$*Li_2CO_2 + 2CO_2 + 2Li$	**(2) ⇌ (3)**	-1.95	-2.31	-1.81	1.95	2.31	1.81
(4)	$*LiCO_3 + *CO + 3Li + CO_2$	**(3) ⇌ (4)**	0.61	0.62	0.36	-0.61	-0.62	-0.36
(5)	$*LiCO_3 + CO + 3Li + CO_2$	**(4) ⇌ (5)**	3.74	3.97	3.89	-3.74	-3.97	-3.89
(6)	$*Li_2CO_3 + CO + CO_2 + 2\ Li$	**(5) ⇌ (6)**	-3.35	-4.21	-4.07	3.35	4.21	4.07
(7)	$*Li_2CO_3 + *CO + CO_2 + 2Li$	**(6) ⇌ (7)**	-2.9	-1.84	-1.45	2.9	1.84	1.45
(8)	$Li_2CO_3 + *CO + CO_2 + 2\ Li$	**(7) ⇌ (8)**	3.15	3.13	1.87	-3.15	-3.13	-1.87
(9)	$*COLi + Li + CO_2 + Li_2CO_3$	**(8) ⇌ (9)**	-0.56	-1.48	0.26	0.56	1.48	-0.26
(10)	$*C + *Li_2CO_3 + Li_2CO_3$	**(9) ⇌ (10)**	-2.78	-2.72	-2.48	2.78	2.72	2.48
(11)	$*C + 2Li_2CO_3$	**(10) ⇌ (11)**	2.62	2.45	1.78	-2.62	-2.45	-1.78
	Path 2							
(0)	$3\ CO_2 + 4\ Li$							
(1)	$*CO_2 + 2CO_2 + 4\ Li$	**(0) ⇌ (1)**	-0.16	-0.24	0.19	0.16	0.24	-0.19
(2)	$*C_2O_4 + 4\ Li + CO_2$	**(1) ⇌ (2)**	0.74	0.98	0.64	-0.74	-0.98	-0.64
(3)	$*LiC_2O_4 + 3Li + CO_2$	**(2) ⇌ (3)**	-2.39	-2.6	-1.96	2.39 [a]	2.6 [a]	1.96
(4)	$*Li_2C_2O_4 + CO_2 + 2\ Li$	**(3) ⇌ (4)**	-1.8	-1.93	-1.97	1.8	1.93	1.97 [a]
(5)	$Li_2C_2O_4 + CO_2 + 2\ Li$	**(4) ⇌ (5)**	1.61	1.79	1.1	-1.61	-1.79	-1.1
(6)	$*LiCO_3 + *C + Li + Li_2CO_3$	**(5) ⇌ (6)**	-1.8	-2.29	-0.88	1.8	2.29	0.88
(7)	$*Li_2CO_3 + *C + Li_2CO_3$	**(6) ⇌ (7)**	-2.12	-2.36	-1.77	2.12	2.36	1.77
(8)	$*C + 2Li_2CO_3$	**(7) ⇌ (8)**	2.62 [a]	2.45 [a]	1.78 [a]	-2.62	-2.45	-1.78
	Path 3							
(0)	$3\ CO_2 + 4\ Li$							
(1)	$*CO_2 + 2CO_2 + 4\ Li$	**(0) ⇌ (1)**	-0.16	-0.24	0.19	0.16	0.24	-0.19
(2)	$*2CO_2 + 4\ Li + CO_2$	**(1) ⇌ (2)**	-0.03	0.15	0.29	0.03	-0.15	-0.29
(3)	$*LiCO_3 + *CO + 3\ Li + CO_2$	**(2) ⇌ (3)**	-3.03	-3.41	-3.15	3.03	3.41	3.15
(4)	$*Li_2CO_3 + *CO + 2\ Li + CO_2$	**(3) ⇌ (4)**	-2.51	-2.08	-1.63	2.51	2.08	1.63
(5)	$Li_2CO_3 + *CO + 2\ Li + CO_2$	**(4) ⇌ (5)**	3.15	3.13	1.87	-3.15	-3.13	-1.87
(6)	$*COLi + Li + CO_2 + Li_2CO_3$	**(5) ⇌ (6)**	-0.56	-1.48	0.26	0.56	1.48	-0.26
(7)	$*C + *Li_2CO_3 + Li_2CO_3$	**(6) ⇌ (7)**	-2.78	-2.72	-2.48	2.78	2.72	2.48
(8)	$*C + 2Li_2CO_3$	**(7) ⇌ (8)**	2.62	2.45	1.78	-2.62	-2.45	-1.78

Note: value with [a] represents the rate-determining-step. For the discharging process, the step-by-step direction is →, for example: (0) → (1), while for the charging process, the step-by-step direction is ←.

References

1. Li, Y.; Yang, C.; Yue, J.; Cong, H.; Luo, W. Polymorphism-Interface-Induced Work Function Regulating on Ru Nanocatalyst for Enhanced Alkaline Hydrogen Oxidation Reaction. *Adv. Funct. Mater.* **2023,** *33* (13), 2211586.

2. Yuan, M.; Bai, Y.; Zhang, J.; Zhao, T.; Li, S.; He, H.; Liu, Z.; Wang, Z.; Zhang, G. Work Function Regulation of Nitrogen-Doped Carbon Nanotubes Triggered by Metal Nanoparticles for Efficient Electrocatalytic Nitrogen Fixation. *J. Mater. Chem. A* **2020,** *8* (48), 26066-26074.

3. Lian, Z.; Lu, Y.; Wang, C.; Zhu, X.; Ma, S.; Li, Z.; Liu, Q.; Zang, S. Single-Atom Ru Implanted on Co_3O_4 Nanosheets as Efficient Dual-Catalyst for Li-CO_2 Batteries. *Adv. Sci.* **2021,** *8* (23), e2102550.

4. Cheng, J.; Bai, Y.; Lian, Y.; Ma, Y.; Yin, Z.; Wei, L.; Sun, H.; Su, Y.; Gu, Y.; Kuang, P.; Zhong, J.; Peng, Y.; Wang, H.; Deng, Z. Homogenizing Li_2CO_3 Nucleation and Growth Through High-Density Single-Atomic Ru Loading Toward Reversible Li-CO_2 Reaction. *ACS Appl. Mater. Interfaces* **2022,** *14* (16), 18561-18569.

5. Lin, J.; Ding, J.; Wang, H.; Yang, X.; Zheng, X.; Huang, Z.; Song, W.; Ding, J.; Han, X.; Hu, W. Boosting Energy Efficiency and Stability of Li-CO_2 Batteries via Synergy Between Ru Atom Clusters and Single-Atom Ru-N_4 Sites in the Electrocatalyst Cathode. *Adv. Mater.* **2022,** *34* (17), e2200559.

6. Wang, J.-H.; Zhang, Y.; Liu, M.; Gao, G.-K.; Ji, W.; Jiang, C.; Huang, X.; Chen, Y.; Li, S.-L.; Lan, Y.-Q. Single-Metal Site-Embedded Conjugated Macrocyclic Hybrid Catalysts Enable Boosted CO_2 Reduction and Evolution Kinetics in Li-CO_2 Batteries. *Cell Rep. Phys. Sci.* **2021,** *2* (10), 100583.

7. Wang, Y.; Zhou, J.; Lin, C.; Chen, B.; Guan, Z.; Ebrahim, A. M.; Qian, G.; Ye, C.; Chen, L.; Ge, Y.; Yun, Q.; Wang, X.; Zhou, X.; Wang, G.; Li, K.; Lu, P.; Ma, Y.; Xiong, Y.; Wang, T.; Zheng, L.; Chu, S.; Chen, Y.; Wang, B.; Lee, C. S.; Liu, Y.; Zhang, Q.; Fan, Z. Decreasing the Overpotential of Aprotic Li-CO_2 Batteries with the in-Plane Alloy Structure in Ultrathin 2D Ru-Based Nanosheets. *Adv. Funct. Mater.* **2022,** *32* (30), 2202737.

8. Deng, Q.; Yang, Y.; Yin, K.; Yi, J.; Zhou, Y.; Zhang, Y. Boosting Active Species Ru-O-Zr/Ce Construction at The Interface of Phase-Transformed Zirconia-Ceria Isomerism toward Advanced Catalytic Cathodes for Li-CO_2 Batteries. *Adv. Energy Mater.* **2023,** *13* (40), 2302398.

9. Cheng, Z.; Fang, Y.; Yang, Y.; Zhang, H.; Fan, Z.; Zhang, J.; Xiang, S.; Chen, B.; Zhang, Z. Hydrogen-Bonded Organic Framework to Upgrade Cycling Stability and Rate Capability of Li-CO_2 Batteries. *Angew. Chem. Int. Ed. Engl.* **2023,** *135* (45), e202311480.

10. Naik, K. M.; Chourasia, A. K.; Shavez, M.; Sharma, C. S. Bimetallic RuNi Electrocatalyst Coated MWCNTs Cathode for an Efficient and Stable Li-CO_2 And Li-$CO_{2\ Mars}$ Batteries Performance with Low Overpotential. *Chemsuschem.* **2023,** *16* (18), e202300734.

11. Savunthari, K. V.; Chen, C. H.; Chen, Y. R.; Tong, Z.; Iputera, K.; Wang, F. M.; Hsu, C. C.; Wei, D. H.; Hu, S. F.; Liu, R. S. Effective Ru/CNT Cathode for Rechargeable Solid-State Li-CO_2 Batteries. *ACS Appl. Mater. Interfaces* **2021,** *13* (37), 44266-44273.

12. Zou, J.; Liang, G.; Yuwono, J. A.; Zhang, F.; Fan, Y.; Zhang, S.; Johannessen, B.; Sun, L.; Guo, Z. Size-Dependent Effects of Ru Nanoparticles on Li-CO_2 Batteries. *ACS Energy Lett.* **2024,** *9* (10), 5145-5155.

13. Ma, Y.; Qu, H.; Wang, W.; Guo, Z.; Yu, Y.; Liu, F.; Yu, B.; Tian, M.; Li, Z.; Li, B.; Wang, L. Graphdiyne Scaffold Anchored Highly Dispersed Ruthenium Nanoparticles As an Efficient Cathode Catalyst for Rechargeable Li–CO_2 Battery. *Chin. Chem. Lett.* **2024,** *35* (1), 108352.

14. Ye, X.; Liu, W.; Lu, Y.; Zheng, X.; Bi, Y.; Zheng, M.; Han, L.; Liu, B.; Ning, Y.; Jafri, S. H. M.; Zhao, X.; He, S.; Zhang, S.; Li, H. Graphene Nanoribbons/Ru As Efficient Cathodic Catalysts for High-Performance Rechargeable Li–CO_2 Batteries. *J. Mater. Chem. A.* **2024,** *12* (18), 10713-10725.

15. Jian, T.; Ma, W.; Hou, J.; Ma, J.; Li, X.; Gao, H.; Xu, C.; Liu, H. Alloy/Layer Double Hydroxide Interphasic Synergy via Nano-Heterointerfacing for Highly Reversible CO_2 Redox Reaction in Li-CO_2 Batteries. *Nano Res.* **2024,** *17* (6), 5206-5215.

16. Ma, W. Q.; Hou, J. G.; Liu, S. Y.; Jian, T. Z.; Ma, J. P.; Xu, C. X.; Liu, H. Transforming Cu into Cu_2O/RuAl Intermetallic Heterojunction for Lowering the Thermodynamic Energy Barrier of the CO_2 Reduction and Evolution Reactions in Li-CO_2 Battery. *J. Energy Chem.* **2024,** *98*, 531-540.

17. Zhao, J.; Xu, X.; Chen, J.; Liu, Y.; Wu, J.; Lou, F.; Fan, Y.; Qiao, Y. Ultrafine Ru Nanoparticles Anchored on N-Doped Mesoporous Hollow Carbon Spheres as a Highly Efficient Bifunctional Catalyst for Li–CO_2 Batteries. *J. Power Sources* **2024,** *607*, 234577.

18. Zhou, J.; Xu, Z.; Cui, K.; Yin, J. A.; Chen, H. C.; Wang, Y.; Liu, F.; Wang, T.; Hao, F.; Xiong, Y.; Wang, C.; Ma, Y.; Lu, P.; Yin, J.; Guo, L.; Meng, X.; Ye, C.; Ming Chen, H.; Zhu, Y.; Lu, J.; Fan, Z. Theory-Guided Design of Unconventional Phase Metal Heteronanostructures for Higher-Rate Stable Li-CO_2 and Li-Air Batteries. *Angew. Chem., Int. Ed. Engl.* **2024**, e202416947.

19. Hao, Q. Q.; Cai, Z. P.; Zhao, X. H.; Wang, L. Y.; Wang, K. X.; Chen, J. S. Boosting the Efficiency and Stability of Li-CO_2 Batteries via a Ruthenium-Based Olefin-Metathesis Catalyst. *J. Am. Chem. Soc.* **2024,** *146* (40), 27802-27808.

20. Jian, T.; Ma, W.; Hou, J.; Ma, J.; Xu, C.; Liu, H. From Ru to RuAl intermetallic/Ru Heterojunction: Enabling High Reversibility of the CO_2 Redox Reaction in Li–CO_2 Battery Based on Lowered Interface Thermodynamic Energy Barrier. *Nano Energy* **2023,** *118*, 108998.

21. Li, S.; Wang, J.-H.; Dong, L.-Z.; Zhang, Y.; Yao, X.-M.; Chen, Y.; Li, S.-L.; Lan, Y.-Q. Three-in-One Fe-Porphyrin Based Hybrid Nanosheets for Enhanced CO_2 Reduction and Evolution Kinetics In Li-CO_2 Battery. *Chin. Chem. Lett.* **2023,** *34* (6), 107633.

22. Wang, Z.; Liu, B.; Yang, X.; Zhao, C.; Dong, P.; Li, X.; Zhang, Y.; Doyle-Davis, K.; Zeng, X.; Zhang, Y.; Sun, X. Dual Catalytic Sites of Alloying Effect Bloom CO_2 Catalytic Conversion for Highly Stable Li–CO_2 Battery. *Adv. Funct. Mater.* **2023,** *33* (28), 2213931.

23. Lian, Z.; Pei, Y.; Ma, S.; Lu, Y.; Liu, Q. Anchoring Ru/RuO_2Nanoparticles on Porous Carbon Shell As an Efficient Cathode Catalyst for Li-CO_2 Battery. *ChemistrySelect* **2022,** *7* (7), e202104549.

24. Lian, Z.; Lu, Y.; Ma, S.; Wang, L.; Li, Z.; Liu, Q. An Integrated Strategy For Upgrading Li-CO_2 Batteries: Redox Mediator and Separator Modification. *Chem. Eng. J.* **2022,** *450*.

25. Fan, L.; Shen, H.; Ji, D.; Xing, Y.; Tao, L.; Sun, Q.; Guo, S. Biaxially Compressive Strain in Ni/Ru Core/Shell Nanoplates Boosts Li-CO_2 Batteries. *Adv. Mater.* **2022,** *34* (30), e2204134.

26. Zhang, Z.; Bai, W. L.; Cai, Z. P.; Cheng, J. H.; Kuang, H. Y.; Dong, B. X.; Wang, Y. B.; Wang, K. X.; Chen, J. S. Enhanced Electrochemical Performance of Aprotic Li-CO_2 Batteries with a Ruthenium-Complex-Based Mobile Catalyst. *Angew. Chem.* **2021,** *133* (30), 16540-16544.

27. Thoka, S.; Tsai, C. M.; Tong, Z.; Jena, A.; Wang, F. M.; Hsu, C. C.; Chang, H.; Hu, S. F.; Liu, R. S. Comparative Study of Li-CO_2 and Na-CO_2 Batteries with Ru@CNT As a Cathode Catalyst. *ACS Appl. Mater. Interfaces* **2021,** *13* (1), 480-490.

28. Xing, Y.; Wang, K.; Li, N.; Su, D.; Wong, W.-T.; Huang, B.; Guo, S. Ultrathin RuRh Alloy Nanosheets Enable High-Performance Lithium-CO_2 Battery. *Matter* **2020,** *2* (6), 1494-1508.

29. Wang, C.; Shang, Y.; Lu, Y.; Qu, L.; Yao, H.; Li, Z.; Liu, Q. Photoinduced Homogeneous RuO_2 Nanoparticles on TiO_2 Nanowire Arrays: A High-Performance Cathode Toward Flexible Li–CO_2 Batteries. *J. Power Sources* **2020,** *475* (1), 228703.

30. Qiao, Y.; Wu, J.; Zhao, J.; Li, Q.; Zhang, P.; Hao, C.; Liu, X.; Yang, S.; Liu, Y. Synergistic Effect of Bifunctional Catalytic Sites and Defect Engineering for High-Performance Li–CO_2 Batteries. *Energy Stor. Mater.* **2020,** *27*, 133-139.

31. Qiao, Y.; Xu, S.; Liu, Y.; Dai, J.; Xie, H.; Yao, Y.; Mu, X.; Chen, C.; Kline, D. J.; Hitz, E. M.; Liu, B.; Song, J.; He, P.; Zachariah, M. R.; Hu, L. Transient, in Situ Synthesis of

Ultrafine Ruthenium Nanoparticles for a High-Rate Li–CO_2 Battery. *Energy Environ. Sci.* **2019,** *12* (3), 1100-1107.

32. Bie, S.; Du, M.; He, W.; Zhang, H.; Yu, Z.; Liu, J.; Liu, M.; Yan, W.; Zhou, L.; Zou, Z. Carbon Nanotube@RuO_2 As a High Performance Catalyst for Li-CO_2 Batteries. *ACS Appl. Mater. Interfaces* **2019,** *11* (5), 5146-5151.

33. Zhao, H.; Li, D.; Li, H.; Tamirat, A. G.; Song, X.; Zhang, Z.; Wang, Y.; Guo, Z.; Wang, L.; Feng, S. Ru Nanosheet Catalyst Supported by Three-Dimensional Nickel Foam As a Binder-Free Cathode for Li–CO_2 Batteries. *Electrochim. Acta* **2019,** *299*, 592-599.

34. Guo, Z.; Li, J.; Qi, H.; Sun, X.; Li, H.; Tamirat, A. G.; Liu, J.; Wang, Y.; Wang, L. A Highly Reversible Long-Life Li-CO_2 Battery with a RuP_2-Based Catalytic Cathode. *Small* **2019,** *15* (29), e1803246.

35. Li, X.; Wang, H.; Chen, Z.; Xu, H. S.; Yu, W.; Liu, C.; Wang, X.; Zhang, K.; Xie, K.; Loh, K. P. Covalent-Organic-Framework-Based Li-CO_2 Batteries. *Adv. Mater.* **2019,** *31* (48), e1905879.

36. Zhang, Z.; Yang, C.; Wu, S.; Wang, A.; Zhao, L.; Zhai, D.; Ren, B.; Cao, K.; Zhou, Z. Exploiting Synergistic Effect By Integrating Ruthenium–Copper Nanoparticles Highly Co-Dispersed on Graphene As Efficient Air Cathodes for Li–CO_2 Batteries. *Adv. Energy Mater.* **2019,** *9* (8), 1802805.

37. Jin, Y.; Chen, F.; Wang, J.; Johnston, R. L. Tuning Electronic and Composition Effects in Ruthenium-Copper Alloy Nanoparticles Anchored on Carbon Nanofibers for Rechargeable Li-CO_2 Batteries. *Chem. Eng. J.* **2019,** *375*, 121978.

38. Yang, S.; Qiao, Y.; He, P.; Liu, Y.; Cheng, Z.; Zhu, J.-j.; Zhou, H. A Reversible Lithium–CO_2 Battery with Ru Nanoparticles As a Cathode Catalyst. *Energy Environ. Sci.* **2017,** *10* (4), 972-978.